MACHINE LEARNING FOR PREDICTING MECHANICAL BEHAVIOR OF CONCRETE BEAMS WITH 3D PRINTED TPMS

Kim Tran-Quoc[1,2,3], **Lieu B. Nguyen**[4], **Van Hai Luong**[2,3], **H. Nguyen-Xuan**[1,*]

[1]*CIRTech Institute, HUTECH University, Ho Chi Minh City 700000, Vietnam*
[2]*Faculty of Civil Engineering, Ho Chi Minh City University of Technology (HCMUT),*
268 Ly Thuong Kiet Street, District 10, Ho Chi Minh City, Vietnam
[3]*Vietnam National University Ho Chi Minh City, Linh Trung Ward,*
Thu Duc City, Ho Chi Minh City, Vietnam
[4]*Faculty of Civil Engineering, Ho Chi Minh City University of Technology and Education*
(HCMUTE), Ho Chi Minh City, Vietnam
*E-mail: ngx.hung@hutech.edu.vn

Abstract. Bioinspired structures are remarkable porous structures with great strength-to-weight ratios. Hence, they have been applied in various fields including biomedical, transportation, and aerospace materials, etc. Recent studies have shown the significant impact of the plastic 3D printed triply periodic minimal surfaces (TPMS) structure on the cement beam including increasing the peak load, reducing the deflection, and improving the ductility. In this study, a machine learning (ML) surrogate model has been conducted to predict the beam behavior under static bending load. At first, various combinations of plastic volume fractions and numbers of core layers have been adopted to reinforce the constituent beam. The finite element method (FEM) was implemented to investigate the influences of these reinforcement strategies. Next, the above data were employed to create the ML model. A three-process assessment was proposed to achieve the most suitable model for the present problem, these processes were the model hyperparameter tuning, the performance assessment, and the handling overfitting with deep learning (DL) techniques. Consequently, both beam peak loads and maximum deflections were proportional to the volume fraction. The increment in TPMS layers could lead to the enhancement in both traits but with a nonlinear relationship. Furthermore, each trait may be a ceiling value that could not be exceeded with a specific volume fraction despite any number of layers. This conclusion was indicated by the surrogate model predictions. The final model in this study could deal with noisy data from FEM and with the support of a new early stopping condition, excellent performance could be found on both train and test data. The maximum deviations of 2.5% and 3.5% for peak loads and maximum midpoint displacements, respectively, have verified the robustness of the present surrogate model.

Keywords: TPMS Primitive reinforced beam, TPMS layers, volume fraction, machine learning.

1. INTRODUCTION

Since first commercially developed in the 19th century, reinforced concrete materials have been widely applied to most civil structures. The ductility of the concrete material seemed to be increased by the reinforcement rebars. However, these rebars are commonly made of steel, probably known as a high-density and strongly corrosive material. Difference types of materials have been studied to replace steel. Recently, recycled plastic appeared to be a good solution to this problem. Many reinforcement methods have been developed to apply plastic material to structures. Salazar et al. [1] studied the ductility enhancement of the concrete beam behavior using lattice structures, and the result indicated that the higher plastic ratio leads to better performance in flexure and less compressive strength. The non-uniform lattice was reported to be an advanced method for improving the ductility and energy absorption of the beam structure while using fewer materials [2]. The mentioned lattice was noted as a typical crystal structure, which could also be found in nature and so-called bioinspired structures. Several members of this type could be listed as multi-cell tubes, helicoidal tubes, honeycomb, and hierarchical foam, etc [3]. Among others, triply periodic minimal surface (TPMS) structures were suggested as remarkable ones. The key characteristic of this structure group was that it is formed by zero-self-intersecting surfaces. This indicated the efficiency in reducing stress concentration on the structure surface. This complex geometry might not be fabricated by traditional manufacturing methods, but with the advancement in additive manufacturing (AM), TPMS structures could be assembled by material printing [4–6].

Therefore, numerous publications have been conducted to investigate the mechanical behaviors of various TPMS structures with different materials based on 3D printing technology. A study by Lee et al. [7] has shown mechanical characteristics of the Primitive TPMS structure, namely the elastic modulus E, bulk modulus K, shear modulus G, anisotropy indexes, compression and shear strength, etc., with respect to its volume fraction. The anisotropic material behaviors of these TPMSs were indicated in the previous work along with the thermal and electrical behavior of the structure [8]. Furthermore, TPMS structures made of metallic material were suggested to have a great value of energy absorption capacity. Different metal 3D printing methods such as selective laser melting (SLM) and selective laser sintering (SLS) were adopted to verify this affirmation [9, 10]. Sheet-based TPMS structures were considered to have greater mechanical behavior than the skeletal-based ones [11]. Yang et al. [12] conducted finite element analysis (FEA) simulations to compute the behavior of these metallic structures with good agreements with experimental results. Consequently, the enhancement in energy absorption has been reported to be valuable. This conclusion was verified by Tran et al. [13] with impact loads and Peng et al. [14] with explosive loads. The sandwich plates with plastic TPMS cores in these studies have great energy absorption capacity under dynamic load.

However, the above studies used either the finite element method (FEM) or experiment to investigate the TPMS structures due to the lack of appropriate theoretical models. Recently, the authors have conducted a research on this issue [15]. A new curve-fitting model for cellular material's behaviors has been proposed which was a two-phase piece-wise function. This approach has shown its efficiency in predicting the mechanical

properties of metallic TPMS structures. Furthermore, a new functionally graded TPMS (FG-TPMS) plate has also been revealed with various porosity distribution functions. The results showed that with the gradation approach, the TPMS plates have been remarkably improved with all free vibration, buckling, and static responses.

Moreover, recycled plastic material is possibly one of the most suitable materials for the aquatic environment. Based on this affirmation, Dang et al. [16] have introduced a breakwater solution using TPMS core reinforced cementitious block. An effective reduction of wave effects toward 50% has been indicated by the simulations. In addition, the TPMS geometry has also been adopted to reinforce the beam structures. Nguyen-van et al. [17] have revealed the comparison between two TPMS reinforced cement beams, the plastic molds cement beam, and the plain cement beam. It is claimed that the reinforced beams might provide excellent influences on the peak load and the flexural stiffness under static bending load. As in the later investigation of the same authors, an increment in energy absorption capacity of this beam subjected to dynamic load has been indicated with the value of 33% [18]. On the other hand, previous studies chiefly investigate the effectiveness of the plastic TPMS core in beam structures regardless of assessing the influence of various core parameters on the beam behaviors. As a reinforcement component, the plastic TPMS core could increase the ductility of concrete materials. Therefore, both ultimate load and maximum deflection of the cement beam could be improved. Consequently, the influence of the TPMS core properties on the cement beam should be achieved for further applications.

However, both experimental and simulation approaches to this structure might be considered challenging, and the complex geometry was noted as the major reason. While 3D printing technology should be employed to manufacture the specimen, relevant fine mesh and material nonlinearity responses were crucial for FEA simulation. For certain TPMS parameters, both the FEA computation time and the experimental time might be time-consuming and uneconomical. This could be a barrier to applying this type of beam in real-world problems. In this work, the above data were used to create a surrogate model based on machine learning (ML) was created. With the rapid development of deep learning (DL) techniques, ML algorithms could be applied in many fields of mechanics as presented in [19, 20]. Prediction application was considered a representation of ML models. For instance, studies about reinforced concrete beam [21], steel-concrete connections [22], high-performance concrete strength [23], reliability of truss structures [24], etc. The typical research about the application of ML to optimization of the truss system was the publication by Nguyen et al. [25]. In this study, the optimization speed was significantly increased compared to other non-gradient optimization algorithms such as metaheuristics. The impacts of the activation function and optimization algorithm on training time have been investigated as well. Therefore, the hyperparameter choosing should be considered attentively. This process is commonly named the hyperparameter tuning process. In this study, a three-process assessment strategy was adopted that both hyperparameter tuning and overfitting handling were included. The ML model can provide an excellent surrogate model for the present problem. Furthermore, the predictions of this model are adopted to generate a deeper analysis of the impact of these TPMS parameters on the beam behaviors.

This study is divided into seven sections as follows. Section **1** introduces the TPMS structures, and their recent applications, and indicated the research contributions. Section **2** provides detailed information about the TPMS geometry, while its main application in this study is proposed in Section **3** which is the plastic TPMS reinforced cement beam. The FEA and the ML models are presented in Sections **4** and **5** respectively. Section **6** demonstrate the results of both FEA simulations and ML surrogate models along with deep discussions on the influences of TPMS parameters on beam behaviors. A brief conclusion can be found in the last section of this study, which is Section **7**. In sum, the contribution of this study can be expressed as two main processes that are the FEM process and the ML process. The flowchart in Fig. **1** shows the workflow to solve the proposed problems.
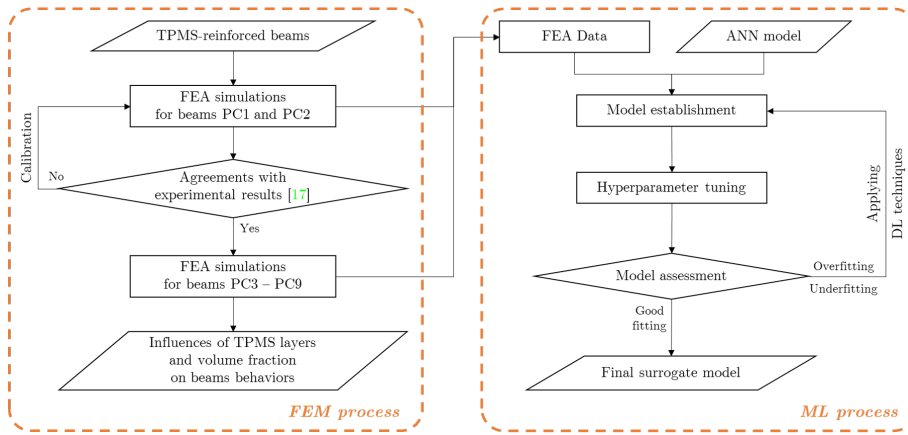

Fig. 1. Flowchart of this study problems

2. TRIPLY PERIODIC MINIMAL SURFACES (TPMS)

A TPMS is the cyclic-repetition combination of minimal surface units in all three perpendicular dimensions. TPMSs are also known as a crystal structure with the basic property of the minimal surface, which is the non-self-intersecting surface and therefore reduces stress concentration affection [26]. Many new TPMS structures have been continuously published since its first discovery. The earliest structures were founded by Herman Schwarz and his student namely Primitive (P), Diamond (D), Hexagonal (H), and Neovius (N). In addition, the Gyroid structure (G) is well known as a bioinspired structure which was revealed by Alan Schoen along with many other TPMS structures based on skeleton graphs of crystal [27]. There are several methods to form the TPMS geometry; however, the implicit function might be considered the most conventional approach [28]. A few common TPMS geometries can be described as follows

- Primitive (P):

$$\phi(x,y,z) = \cos \omega_x x + \cos \omega_y y + \cos \omega_z z, \tag{1}$$

- Gyroid (G):

$$\phi(x,y,z) = \cos \omega_x x \sin \omega_y y + \cos \omega_y y \sin \omega_z z + \cos \omega_z z \sin \omega_x x, \tag{2}$$

- Diamond (D):

$$\phi(x, y, z) = \sin \omega_x x \sin \omega_y y \sin \omega_z z + \sin \omega_x x \cos \omega_y y \cos \omega_z z$$
$$+ \cos \omega_x x \sin \omega_y y \cos \omega_z z + \cos \omega_x x \cos \omega_y y \sin \omega_z z, \tag{3}$$

- I-graph and wrapped package-graph (IWP):

$$\phi(x, y, z) = 2 \left(\cos \omega_x x \cos \omega_y y + \cos \omega_y y \cos \omega_z z + \cos \omega_z z \cos \omega_x x \right)$$
$$- \left(\cos 2\omega_x x + \cos 2\omega_y y + \cos 2\omega_z z \right), \tag{4}$$

with

$$\omega_i = 2\pi \frac{n_i}{L_i} | i = x, y, z, \tag{5}$$

where x, y, z are the axes of the three-dimensional Cartesian coordinate system; ω_i are the periodicities of the TPMS function; L_i are the unit cell lengths along the corresponding axis; n_i are the numbers of unit cells along the corresponding axis.

(a) Primitive

(b) Gyroid

(c) Diamond

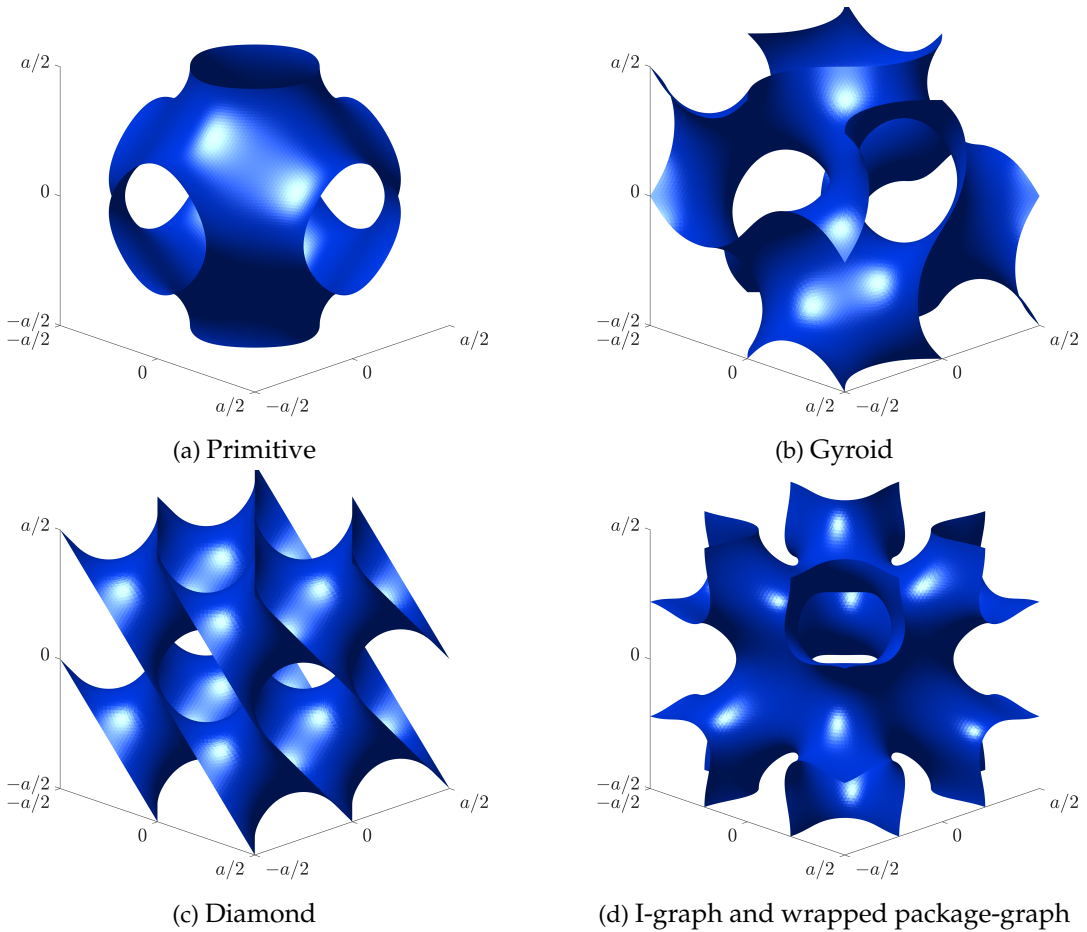(d) I-graph and wrapped package-graph

Fig. 2. Typical TPMS structures

In this study, the uniform TPMSs were adopted where the properties of the surface in all three spatial dimensions are the same ($\omega_i = \omega, n_i = 1, L_i = a$). The geometries of above mentioned TPMS types are shown in Fig. 2.
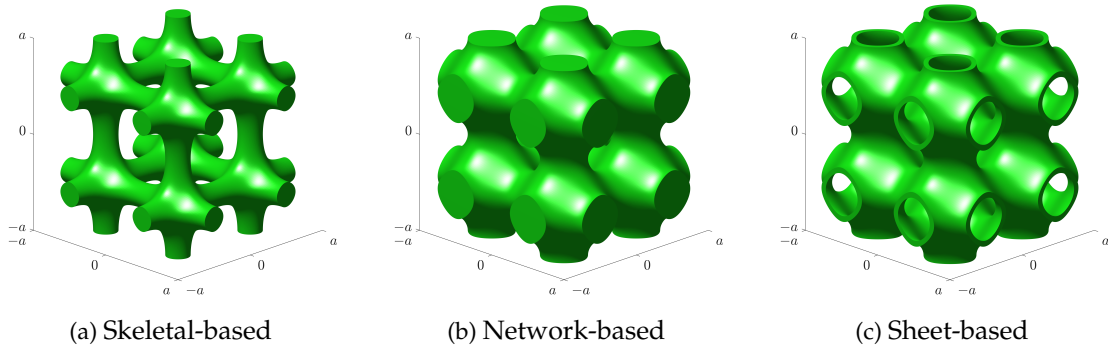

(a) Skeletal-based   (b) Network-based   (c) Sheet-based

Fig. 3. Several Primitive solid types

The majority of TPMS should divide its surrounding cube into two parts that are even in volume. In other words, the volume fraction between a network-based TPMS solid and its cube is equal to 50%. However, there are plenty of solid types that can be created from a specific TPMS. For illustrations, three types of Primitive TPMS solids are shown in Fig. 3 including skeletal-based, network-based, and sheet-based solids. These solid types can be created by adopting different modification methods in the implicit function. Furthermore, the volume fraction of the structure can be simply controlled by the control parameter (t) in the modified implicit functions. In this study, the sheet-based solid Primitive TPMS was utilized for further investigations. Eq. (6) describes the sheet-based solid implicit function.

$$-t \leq \phi(x, y, z) \leq t. \tag{6}$$

Bioinspired structures continuously show their high performances in many applications because they have been subjected to numerous evolution factors as well as have been gradually optimized through time. The TPMS structure is also denoted as a group of bioinspired structures. In fact, they can be found in various natural aspects namely butterfly wings, sea urchins, nano-porous gold, human bone, etc. A demonstration of this natural origin can be found in Fig. 4.

One of the outstanding characteristics of these TPMSs is that both their area and volume are well optimized and therefore minimizing the self-mass. Moreover, to ensure the mobility of the organism, these structures have to provide incredible strength and stiffness. Consequently, the high stiffness-to-weight or strength-to-weight ratio of these structures was the most important feature that leads to their wide-range applications. For instance, TPMS structures have been widely used in medical equipment and body implants since the beginning. In addition to their high stiffness, the reducing-concentration-stress property of these structures could attract a large number of researchers who mainly focused on their mechanical behaviors. Many scientific reports on the responses of metallic TPMS structures have been published [11,12,30]. The results showed that this type of
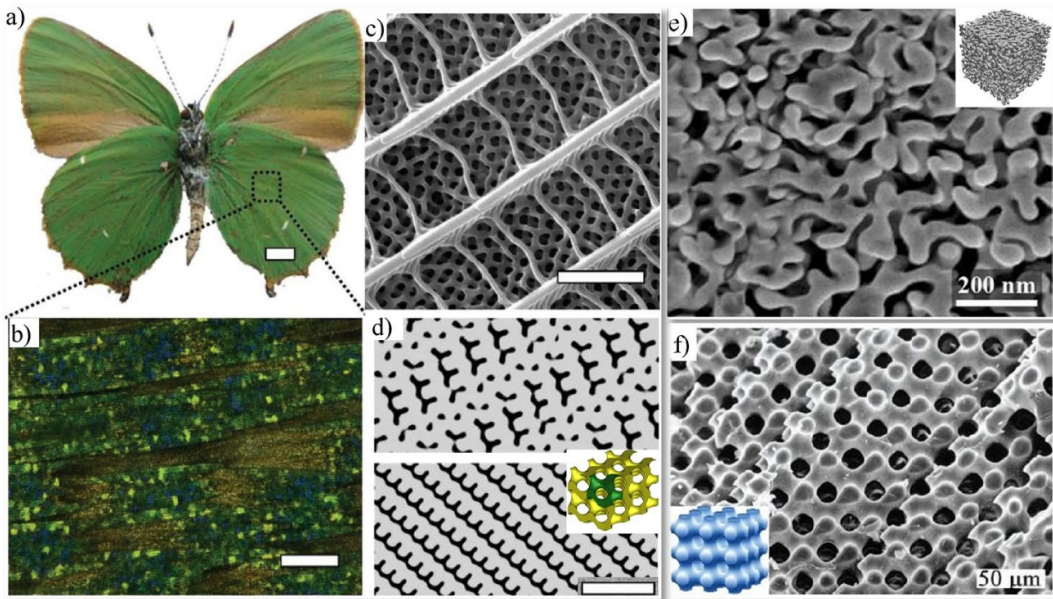
Fig. 4. TPMS structures in nature, a)-d) the Gyroid structure in butterfly wing, e) the Fischer-Koch structure in nano-porous gold, and f) the Primitive structure in sea urchin microstructure [29]

structure can be used to replace the traditional lattice structure or crystal structure. Recently, several articles on lightweight concrete beams and slabs reinforced by 3D printed TPMS shell made of recycled plastic materials have been published with different load types such as static loads [17, 31], dynamic load [18], impulsive load [13, 14], wave load [16], etc. As a result, it is indicated that these structures show the great potential of using recycled plastic to replace steel material in traditional reinforced concrete beams.

3. BEAM REINFORCED WITH 3D PRINTED TPMS STRUCTURES

3.1. 3D printing technology

With the mentioned excellent characteristics, scientists have been applying these TPMSs in structural members to enhance their performances under various loading schemes. Based on the advances of 3D printing technology, TPMS structures, despite having complex geometry, can still be fabricated. Solid cement beams reinforced with the recycled plastic TPMS core showed efficiency with great improvement in load-bearing capacity and energy absorption compared to other reinforcement strategies.

Additive manufacturing (AM) technology has been being widely developed and applied in various research fields and industries. The more popular name for this technology is 3D printing technology. The primary fabrication method of this technology is that by using equivalent printing devices, a layer of material can be created with a specific height. This layer is further superimposed on top of another layer. This process continues until the 3D built-up specimen is created. This technology is in contrast to the traditional fabrication technology which is known as subtractive manufacturing. Object

identification and layering for fabrication are the most important tasks in 3D printing implementation. With the support of modern software and spatial-model-design formats such as computer-aided design (CAD), standard triangle language (STL), etc., 3D printing technology is being simpler for practical applications. Equipment for printing or spraying materials should be considered attentively corresponding to the manufactured object and its material [5,22]. The most popular 3D printing methods can be found in [32] as follows

- Fused deposition modeling (FDM): Thermoplastic materials are melted and then solidify to create layers;
- Inkjet printing: The ceramic powder is melted and formed into droplets that latter be solidified into layers;
- Powder bed fusion (PDF): Each layer is created by fusing ultra-fine metallic powder with a laser beam or a binder;
- Stereolithography (SLA): The technique that uses an ultraviolet laser to harden the plastic materials which is in liquid form.

In addition, due to the ability of creating sophisticated geometries with high precision, AM technology has been used to fabricate numerous bioinspired structures [3]. It is indicated that these structures bring enormous difficulties in traditional manufacturing methods. Moreover, 3D printing technology allows the product to be created with different materials including metal, plastic, ceramic, cement, etc. This material diversity is also one of the reasons that promote studies on 3D printing technology. Recently, recycled plastic materials have been adopted for investigations and implementations. Several thermoplastics that can be adopted are polylactic acid (PLA), acrylonitrile butadiene styrene (ABS), polycarbonate (PC), etc. More specifically, ABS plastic is employed in this study along with the FDM printing method.

3.2. Effectiveness of plastic TPMS scaffold

Recent studies have shown that the TPMS core could create confinement in the cement beam, thereby increasing the ultimate strain and compressive strength of cement. In addition, TPMS cores printed with ABS or PLA are much lighter than concrete, therefore reducing the overall weight of the structure. This reduction depends on the volume that the TPMS core occupies in the member which is called the volume fraction. The research [1] has shown that the percentage of ABS plastic material of at least 19.2% might reduce the concrete compressive strength by 22%. Therefore, the volume fraction of the TPMS core needs to be considered attentively. In the range of low volume fraction, the sheet-based TPMS solid can be considered the thicken-based TPMS solid. This type of solid is generated by adopting a thickness to the surface (where the control parameter (t) is equal zero). In this study, the TPMS core in simulations is approximated by this approach. The corrosion resistance of plastics is also an advantage compared with steel rebar reinforced beams [16]. Furthermore, to investigate the ductility of the beam, a polymer fiber-reinforced lightweight cement with a content of about 0.25% total volume of the beam was employed [17]. In this study, the Primitive TPMS cores are used to reinforce the cement beam. While the overall dimensions of the beam are constant during

the investigation, the number of TPMS layers and the volume fraction of the core are varied. From the results of these simulations, an excellent surrogate model which is able to predict the beam behavior can be achieved.

In the previous study of Nguyen-van et al. [17], the impact of the TPMS core has been validated with both experiment and Finite Element Analysis simulation. The standard error between simulation and experimental results of one-layer and two-layer beams ranged from 3% to 7%. Besides, the stress-strain curve of the beam shown in Fig. 5 again displays the similarity between simulation and experiment. Consequently, the simulation could capture the responses of the considering beams. In other words, the reliability of the simulation was confirmed.
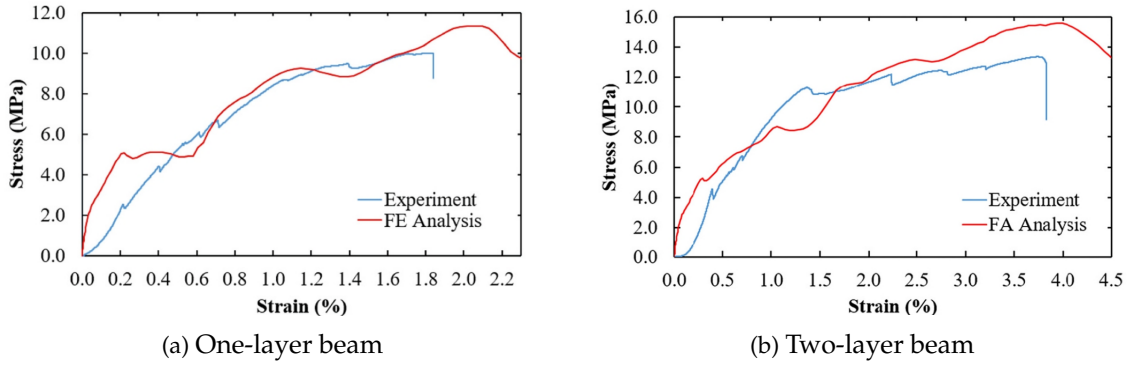
(a) One-layer beam	(b) Two-layer beam

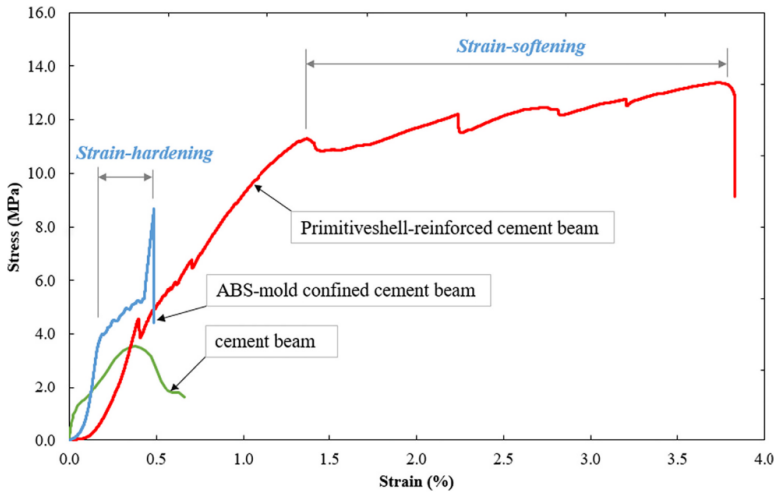*Fig. 5.* Stress-strain curve of one and two-TPMS-layer reinforced beam [17]

Fig. 6. Stress-strain curve of cement beam, ABS-mold confined cement beam, and TPMS shell-reinforced cement beam [17]

In addition, Fig. 6 shows the TPMS core contribution in reducing the brittleness of the cement. This affirmation could be concluded by the beam's plastic behavior and

energy-absorption increment. It should be noted that the strain-softening regime of the beam has appeared, which was similar to the polymer fiber reinforced beam [33]. Thus, both the maximum load and maximum displacement of the beam have increased remarkably compared to the un-reinforced cement beam.

Another result could be found is that an increase in the number of TPMS units might lead to higher improvement in the beam responses. However, as the unit size decreases, the manufacturing process might be more difficult. Moreover, the arrangement of core units could affect the beam behavior as shown in Fig. 7. For instance, the one-layer beam had an incline crack path in the cement part between TPMS units instead of a straight line in the center of the beams. In contrast, the two-layer beam's crack path was similar to the normal cement beam due to the fact that there were not any units at the center of the beam.
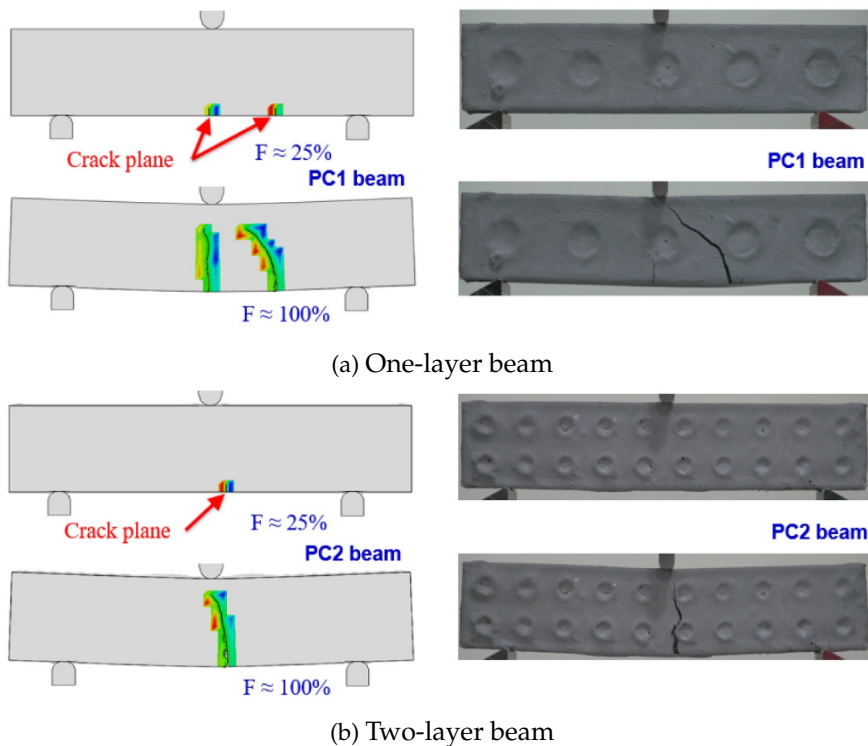

(a) One-layer beam

(b) Two-layer beam

Fig. 7. Crack propagation in TPMS core reinforced beam with 25% and 100% bending load of one and two-layer beam [17]

4. SIMULATION MODEL

4.1. Beam geometry properties

The beam configuration in the previous study is adopted for comparisons as shown in Fig. 8. The 50 mm × 50 mm × 250 mm beam is filled with lightweight cement. The plastic molds and TPMS core are simultaneously fabricated by 3D printing. While the

thickness of the molds is equal to 2mm for all cases, the thickness of the core is varied with the volume fraction of plastic material.
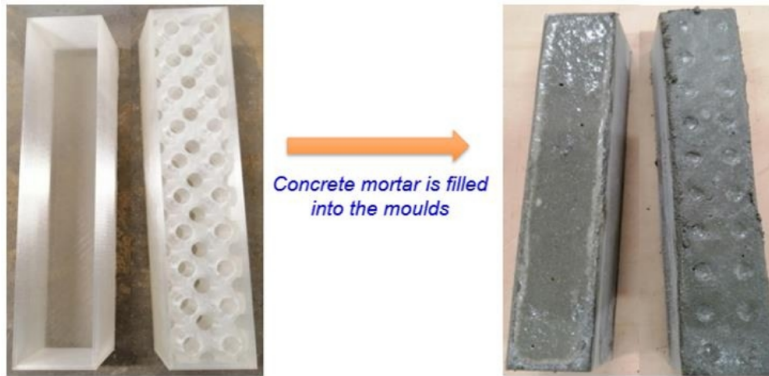

Fig. 8. The 3D printed molds and the cement filled beam [18]

Various reinforcement strategies are employed in this study to investigate the influence of both the number of TPMS layers and the volume fraction of the plastic core on the beam performance. The one, two, and three-layer TPMS cores are included along with the volume fraction range of 10% to 20%. Beam labels and their corresponding parameters are shown in Table 1.

Table 1. The geometric description of TPMS beam's reinforcement core

Volume fraction	Number of TPMS layers		
	1	2	3
10%	PC1	PC2	PC3
15%	PC4	PC5	PC6
20%	PC7	PC8	PC9

Furthermore, by remaining the beam size and changing the number of layers, the relationships between this value, the TPMS unit size, and the total number of TPMS units can be described in Eq. (7)

$$a = \frac{50 \text{ mm}}{n_{layer}}, \quad n_{unit} = 5 \times n_{layer}^3, \tag{7}$$

where a is the TPMS unit size; n_{layer} is the number of TPMS layers; n_{unit} is the total number of TPMS units.

As mentioned in the previous section 3.2, the volume fraction of the TPMS core can be calculated from the mean thickness of the sheet-based structures with the following equation

$$t_{shell} = \frac{VF \times a^3}{A_0} = \frac{VF \times a}{2.3526}, \tag{8}$$

where t_{shell} is the TPMS shell thickness, VF is the volume fraction of the TPMS core; $A_0 = 2.3526 \times a^2$ is the surface area of the Primitive TPMS surface with control parameter equals to zero ($t = 0$) [34].

Table 2. The beam core parameters with various reinforcement strategies

Beam	n_{layer}	VF	a (mm)	n_{unit}	t_{shell} (mm)
PC1	1	10%	50.0	005	2.125
PC2	2	10%	25.0	040	1.063
PC3	3	10%	16.7	135	0.710
PC4	1	15%	50.0	005	3.188
PC5	2	15%	25.0	040	1.594
PC6	3	15%	16.7	135	1.065
PC7	1	20%	50.0	005	4.251
PC8	2	20%	25.0	040	2.125
PC9	3	20%	16.7	135	1.420

The core parameters of the considering beams are provided in Table 2. The static bending load is adopted in this work to assess the beam responses. The load is assigned in the center of the beam according to the three-point bending test diagram with a span of 200 mm. The printing direction behavior might be weaker than other directions due to the effect of the FDM printing method. Therefore, the side face of the beam was used as the load interaction surface. As the result, the test can provide the most precise reinforcement behavior of the TPMS core. The typical simulation model can be seen in Fig. 9.
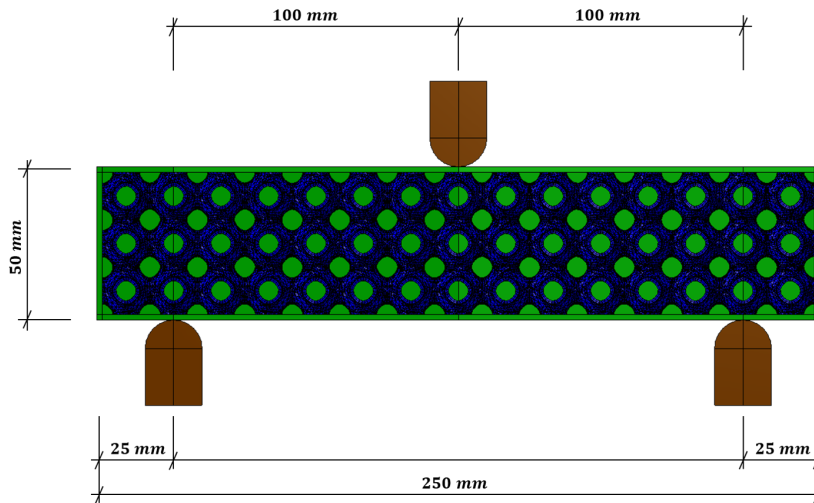

Fig. 9. The bending test simulation of the TPMS reinforced beam

4.2. Materials

The lightweight cement considered in this study is a polymer fiber cement with the mix proportion in Table 3. In the previous research, this cement mixture was utilized to determine the cement mechanical properties with a cubical specimen of 50 mm × 50 mm × 50 mm. This specimen was poured at the same time as the beam and vibrated to ensure that there were not any air bubbles trapped inside. After 28 days of curing in a humid environment, the result of the uniaxial compression test of this cementitious specimen was conducted and is shown in Table 4.

Table 3. Mix proportion of cementitious mortar [17]

Material	Mix design (kg/m^3)
Cement CEM I	550
Fly ash Class F	650
Water	400
Sand	550
PCE admixture	8.45
PVA fiber	0.25% of the total volume

Table 4. Mechanical properties of cementitious mortar [17]

Young modulus, E (MPa)	2500
Mass density, ρ (kg/m^3)	2200
Poisson's ratio, ν	0.2

For brittle materials such as cement, failure occurs when the stress in the cement reaches the yield state and then initializes cracks. The simplified concrete damage plasticity (SCDP) model combines the plasticity theory and the damage theory of concrete. This model is indicated as a suitable model to investigate this type of material [35]. The nonlinear behavior of the material can be described by two factors that are compression damage and tension damage. These damage factors are determined by Eq. (9). In this study, the SCDP model parameters of the cement material are provided from the compression test in the previous study [17] and given in Table 5.

$$d_c = 1 - \frac{\sigma_c}{\sigma_c u},$$
$$d_t = 1 - \frac{\sigma_t}{\sigma_t u}, \tag{9}$$

where σ_c, σ_{cu} are nominal compressive stress and ultimate compressive strength of the material, respectively. σ_t, σ_{tu} are nominal tensile stress and ultimate tensile strength of the material, respectively.

Table 5. SCDP model parameters of cementitious material [17]

Dilation Angle	Eccentricity	Initial Biaxial/Uniaxial Ratio σ_{c0}/σ_{b0}		K Parameter	Viscosity
31	0.1	1.16		0.67	0

Compressive behavior from experiment			Tensile behavior (assumed)		
Yield stress (MPa)	Inelastic strain	Damage parameter, D	Yield stress (MPa)	Cracking strain	Damage parameter, D
23.5	0	0	3.56	0	0
28.1	0.001782	0	0.36	0.017526	0.90
29.9	0.002546	0			
31.0	0.003117	0			
33.6	0.004586	0			
34.6	0.005757	0			
35.2	0.006089	0			
35.6	0.007122	0			
31.3	0.010542	0.12116			
26.7	0.015248	0.25073			
20.8	0.031101	0.41691			
6.4	0.086961	0.82108			
5.9	0.107773	0.83539			

The plastic components of the beam are 3D printed with recycled ABS plastic material. The mechanical characteristics of this common printing material are revealed in Table 6.

Table 6. Mechanical properties of ABS material [17]

Young modulus, E (MPa)	2200
Mass density, ρ (g/mm^3)	1.05
Poisson's ratio, ν	0.2
Yield stress, σ_y (MPa)	56

4.3. Finite element analysis

To study the beam responses, the spatial bending simulation has been utilized along with the nonlinear behavior of the materials. These simulations were conducted in the commercial software using the finite element method (FEM) which was Abaqus/Explicit. In this three-point bending test model, three rigid semi-cylindrical rollers are included together with the beam. These three rollers consist of two test supports and a load transmission device. Several beam models are given in Fig. 10 as an illustration. In addition, the

interaction surface between the support and the beam can be considered a 'hard' contact with a friction coefficient of 0.15 to ensure that the beam cannot have the sliding displacement which is perpendicular to the loading plane. The contact of the beam molds and the cement core is defined as a general contact with the 'hard' normal contact and the tangential contact with a friction coefficient of 1. This friction coefficient value can help the shear stress on this surface vanish. Since then, the failure state of the beam may appear when the stress in the component reaches the yield stress instead of sliding on each other of these two components. Moreover, the similarity in the elastic moduli of both materials, that are 2500 MPa and 2000 MPa for the cement and the plastic, respectively, should also be noted. As the result, the bond-slip effect between these two components can be ignored and considered as a perfect bond [36]. For this reason, the TPMS cores are considered as an embedded member in the beam cementitious part in simulations. Besides, due to the zero-intersecting-surface characteristics of the TPMS shell, the cementitious core might be confined. This behavior is indicated to cause reducing the deviatoric stress and lessening the sliding on the contact surface of the cement core and the TPMS core.
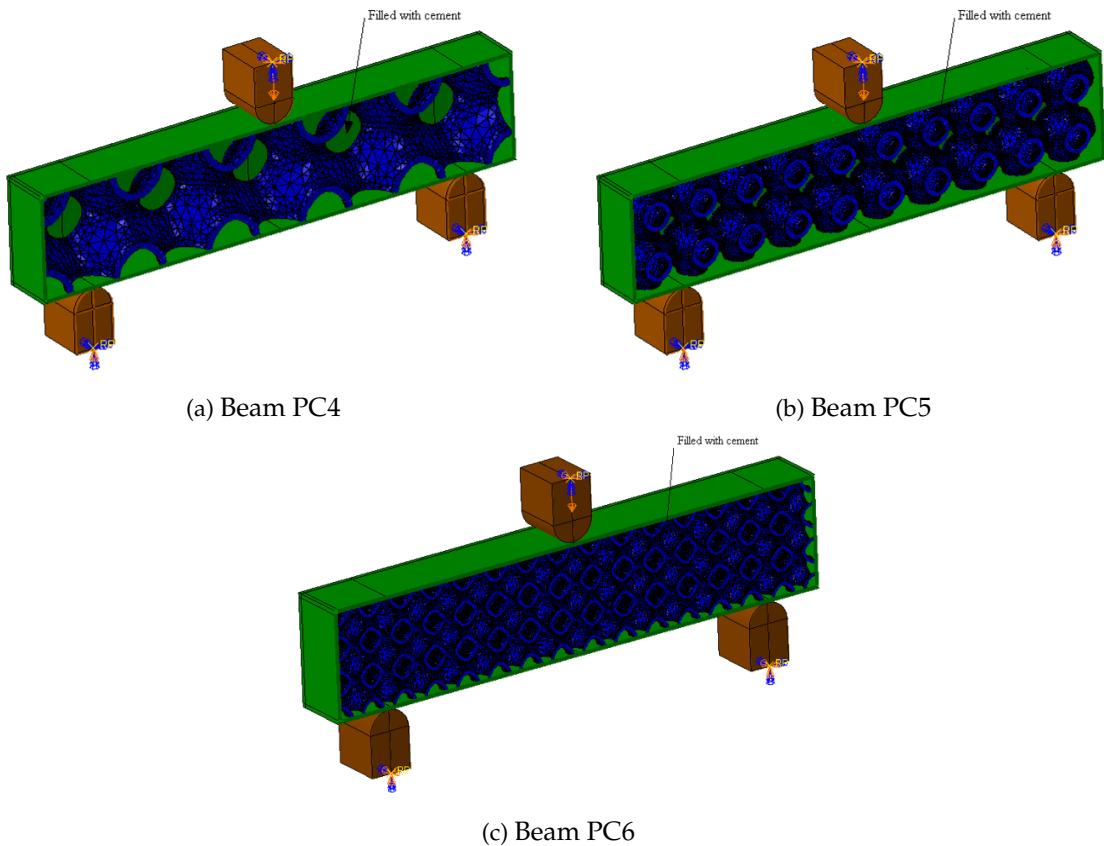

(a) Beam PC4

(b) Beam PC5

(c) Beam PC6

Fig. 10. The three-point bending test simulations of beam (a) PC4, (b) PC5, and (c) PC6

To reduce both computational time and complicated interaction between the load transmission area and the beam, the load of the beam is replaced by the vertical displacement of the load roller. The magnitude of the load is calculated during the simulation process based on the reactions of supports. In this study, the four-node tetrahedral (C3D4) element is adopted to simulate the beam cementitious core. Both the TPMS shell and the molds are modeled by three-node triangular (S3/S3R) elements. The convergence studies on meshing size in previous publications [17, 37] have shown that a 4mm mesh grid could provide acceptable solutions with an optimal computational time. However, this meshing size might not be appropriate for the more-layer beams. For instance, the TPMS unit size is 50mm, 25mm, and 16.7mm for one, two, and three-layer beams, respectively. With the above mesh grid of 4mm for the TPMS shell, the TPMS unit in the three-layer beam is only described by 5 elements which are lesser than other beams. Consequently, the finer meshes should be adopted to produce reliable results for smaller TPMS unit sizes. Another mesh strategy has been proposed in this work to deal with this problem, which is verified in the next section.

5. MACHINE LEARNING APPROACH

Machine learning (ML) is a term used to define computer programs that can produce predictions by using input data. The process to generate the output is called the train-test progress. ML is also known as a subgroup of artificial intelligence (AI). Since the start of the 21st century, applications of AI can be found in almost every aspect of life. Smart devices such as cell phones and computers are typical examples. In addition, with the rapid development of the internet, more and more data are generated all over the world. With these enormous data, ML can be adopted in a wider range. To exploit that huge amount of data more efficiently, the deep learning (DL) technique has been developed to be an effective tool for ML models.

Furthermore, an artificial neural network (ANN) model is a representative of ML algorithms with a multi-layer structure (multi-perceptron), each layer has multiple nodes which can simulate the human nervous system [38] This structure is indicated to lead the ML model to achieved its prediction more accurately and quickly than other traditional approaches namely linear regression, decision tree, etc. With the ability to handle complex problems, the ANN algorithm has grown rapidly and globally. For instance, ANN or ML is commonly used as a surrogate model to reduce computational time in numerous mechanical fields. Besides, these models are further used to predict the mechanical behavior of structures instead of FEA simulations [20]. With a well-trained model, the calculation time can be reduced dramatically from dozens of hours to only a few milliseconds. An ANN model consists of two main progresses, which are the train and the test progress. The results are calculated according to the feed-forward process based on the model parameters (weights and bias) and adjusted through the backpropagation by optimization algorithms. Therefore, the well-trained model is considered an optimal approximation model for the input data. The results are evaluated at the next stage which is the test progress. By assessing these values, the performance of the model can be conducted. As the result, the DL techniques can be adopted to minimize the error and the training time of the model.

5.1. Artificial neural networks

5.1.1. *Architecture*

ANN architecture is configured by three main components: Input data (input layer), computation layers (hidden layer), and output data (output layer). The ANN model is established based on the following definitions and formulas. This architecture can be presented in the diagram as shown in Fig. 11 with nodes denoted as circles and parameters (weights and bias) in form of lines.
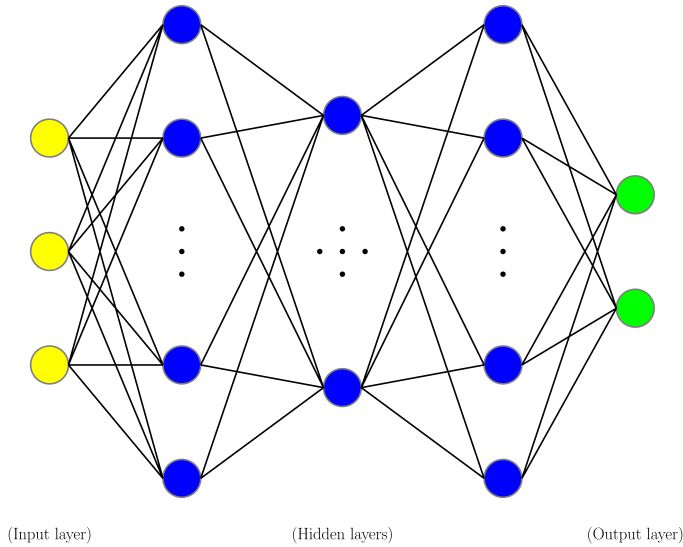

(Input layer)   (Hidden layers)   (Output layer)

Fig. 11. Typical ANN architecture

- Input data is interpreted as a vector of the model variables and is considered as the 0th computational layer of the network, $x = h^{(0)}$;
- An ANN model can have many layers where n is the number of layers, and each computation layer can include many nodes, the number of nodes (excluding the 0th node) of the lth layer is denoted by $d^{(l)}$;
- The connection parameters of nodes (excluding the 0th node) of the $(l-1)^{th}$ layer and the lth layer are denoted by $w^{(l)} \in R^{d^{(l)} \times d^{(l-1)}}$;
- The connection parameters of the 0th node (if any) of the $(l-1)^{th}$ layer and the lth layer is denoted by $b^{(l)} \in R^{d^{(l)}1}$;
- The value of the node in the lth layer is the result of the activation function $f(h^{(l-1)}, \omega^{(l)}, b^{(l)}$ calculated from the node values in the previous $(l-1)^{th}$ layer and the parameter of this layer, defined as Eq. (10);

$$h^{(l)} = f\left(w^{(l)}h^{(l-1)} + b^{(l)}\right) \tag{10}$$

- For instance, for node j of the lth layer presented as Eq. (11);

$$h_j^{(l)} = f\left(\sum_{i=1}^{d^{(l-1)}} w_{ji}^{(l)} h_i^{(l-1)} + b_j^{(l)}\right) \tag{11}$$

- Output data are the results of the model which is the last layer of the network, $y = h^{(n+1)}$;

Defining the model architecture is to determine the number of input variables, output variables, and the number of computational layers as well as the number of nodes in each layer. The total parameters of an ANN network can be calculated based on this structure. In addition, as this number increases, the model may become more complicated. The complexity of the model can bring difficulties in updating the parameters and higher computational costs. The advantage of this heavy model is its significant training accuracy compared to the lighter model. Nevertheless, the higher accuracy on train data may lead to overfitting performance and losing the accuracy on the test data as shown in Fig. 12. Consequently, the model architecture should be decided attentively.
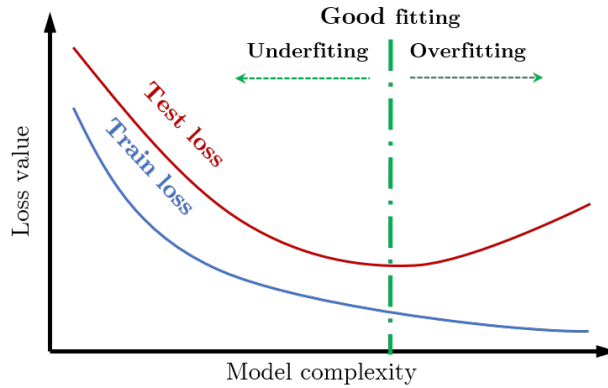

Fig. 12. The influence of architecture complexity on the ANN model performance

5.1.2. *Activation function*

The activation function is used to determine how a node in the network can contribute to a node value in the next layer. The sum products of the node values and the previous layer's parameters can reach a large number (please see Eq. (11) for more detail) which increases the computational time and reduce the reliability of the model. Therefore, the activation function is adopted to improve these problems. Some common activation functions can be used as below and their demonstrations are given in Fig. 13.

- Sigmoid function:

$$f(z) = \frac{1}{1 + e^{-z}} \tag{12}$$

- Tanh function:

$$f(z) = \frac{e^z - e^{-z}}{e^z + e^{-z}} \tag{13}$$

- ReLU function:

$$f(z) = \begin{cases} \alpha(e^z - 1), & z < 0 \\ z. & z \geq 0 \end{cases} \tag{14}$$

- SoftPlus function:

$$f(z) = log(1 + e^z) \tag{15}$$

- 2nd-order Chebyshev polynomial function [25]:

$$f(z) = 2z^2 - 1 \tag{16}$$

- 3rd-order Chebyshev polynomial function [25]:
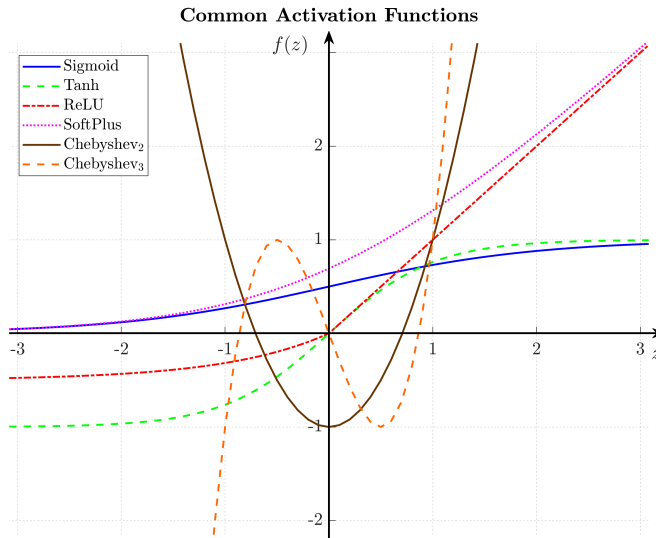
$$f(z) = 4z^3 - 3z \tag{17}$$

Fig. 13. Several common activation functions

In addition, the use of the activation function also helps to create higher-order nonlinearities for the network with fewer computational layers and improve reliability without using more parameters. When using the gradient optimization algorithms, inappropriate activation function may lead to vanishing gradient or exploding gradient at some arbitrary nodes. With a specific problem, the suitable activation function should be adopted through the hyperparameter tuning process. In this study, both model architecture and activation function are achieved simultaneously through the above process.

5.1.3. *Loss function*

The loss function is established based on the deviations between the prediction results from the model and the training dataset. The loss values are employed to verify the model prediction and then to propose solutions to increase that reliability. In this study, the mean square error (MSE) value is adopted as the loss function, where other values including the root mean square error (RMSE) and mean absolute error (MAE) are used as reference metrics. These values are defined by the following functions

$$MSE = \frac{\sum(\boldsymbol{y} - \bar{\boldsymbol{y}})^2}{2m},$$

$$RMSE = \sqrt{\frac{\sum(\boldsymbol{y} - \bar{\boldsymbol{y}})^2}{2m}}, \tag{18}$$

$$MAE = \frac{\sum(|\boldsymbol{y} - \bar{\boldsymbol{y}}|)}{m},$$

where $y, \bar{y}$ are model predictions and input data, respectively; m is the number of input samples.

5.1.4. *Optimization algorithms*

To minimize the loss function, various optimization algorithms (or optimizer) including non-gradient and gradient algorithms can be used to search for the solution and to increase the convergence speed. Since the predicted value y can be calculated based on backpropagation, it can be expressed as a mathematical function in terms of input values x. Therefore, the gradient-based optimizers is noted to be better than others. The basic of gradient optimization algorithms is that the gradient vector represents the direction of decreasing the function value which is also known as the gradient descent. The most important parameter of this theory is the learning rate. With the higher learning rate, the convergence solution may be found faster yet this solution may not be the minimum one as illustrated in Fig. 14.
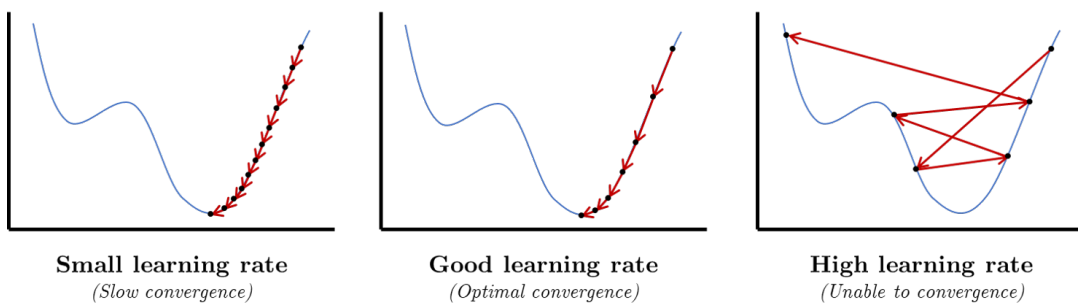

| Small learning rate | Good learning rate | High learning rate |
| *(Slow convergence)* | *(Optimal convergence)* | *(Unable to convergence)* |

Fig. 14. Illustration for the impact of the learning rate on the solution

Furthermore, numerous gradient optimization algorithms have been created namely mini-batch gradient descent (GD), stochastic gradient descent (SGD), root mean squared propagation (RMSprop), adaptive moment estimation (Adam), adaptive gradient algorithm (AdaGrad), adaptive learning rate method (AdaDelta), etc. In these optimizers, the prefix 'Ada' in several optimizers stands for the adaptive algorithms group where the learning rate can be modified during the train process. In addition, to prevent being trapped at the local minimum, the momentum factor has been employed in almost all algorithms. In the ANN model, each time the model uses all the train data is called an epoch. Generally, the train process stops when the epoch reaches the pre-defined maximum epoch. The higher value of this hyperparameter may help the model to find the better solution, however, increase the train time. Along with the maximum epoch, the batch size is also a crucial factor of the train process. The batch size number defines the number of data samples that is used to update the model parameters. The large batch size can cost the longer time for each epoch but shorten the convergence time. However, it is denoted that as the batch size increase, the generality of the model may be reduced. With the small batch size, the model can be updated more frequently but take more epochs to produce the best solution. Several optimizers with different learning rate, batch size and epochs are applied in this study to achieved the most appropriate optimizer hyperparameters for the TPMS beam dataset.

5.1.5. *Data*

As denoted above, data is the key factors of every ML model. A data sample consists of input data and output data. Dataset is the entire samples used in the model which may be divided into three subsets including train dataset, validation dataset, and test dataset. The complexity of the problem is the main aspect that affect the size of the dataset. It is suggested that increasing the dataset could solve the underfit problems. In most cases, the model requires thousands of samples to produce the good results. Furthermore, researchers recently have focused on the noisy data problem where the data may have a large number of incorrect samples. These data are meaningless in the final prediction, however, inhibit the model to find the best solution. Therefore, many DL techniques have been applied to prevent both train loss value and training time to increase in these models. Another technique that is usually used on the dataset is the data scaling. With arbitrary range, the data type can be rescaled into the range of $[a, b]$, normalized into the range of $[0, 1]$, or standardized into the range of $[\sigma - \mu, \sigma + \mu]$. This technique is adopted when the differences in data values are large. For example, with data A $\in [1, 10]$ and B $\in [10^3, 10^4]$, the model tends to optimize the parameters related to data B because the parameters related to data A almost have no effect on the calculation results. By using the data normalization method, or min-max normalize, with the formula in Eq. (19), data are scaled into the range of $[0, 1]$ and the parameters are trained equally when optimizing the model.

$$x_i^{scale} = \frac{x_i - \min(x)}{\max(x) - \min(x)}. \tag{19}$$

In contrast, this study dataset is the combinations of the midpoint displacement, the volume fraction, the number of TPMS layers, and the applied load of the beam. Despite

the volume fraction range of 0 to 1, other data are range of 0 to 10 with 10 is the maximum value of both maximum displacement and peak load. Therefore, the data scaling technique is not applied in this study.

5.2. Model accuracy assessment

The accuracy or the reliability of the model is assessed through the value of the loss function and the correlation graph of this value and the number of epochs which is the convergence history. Three types of model results are shown in Fig. 15 that can be described as follows

- Underfitting: the train or test set provides large errors in results, which cannot be applied to prediction;
- Good fitting: the train and test sets provide small and similar errors; the model is suitable for prediction;
- Overfitting: the train set provides small errors, but the test set offers much larger errors. This result shows that the model prediction is too close to the train data and is difficult in predicting new data.
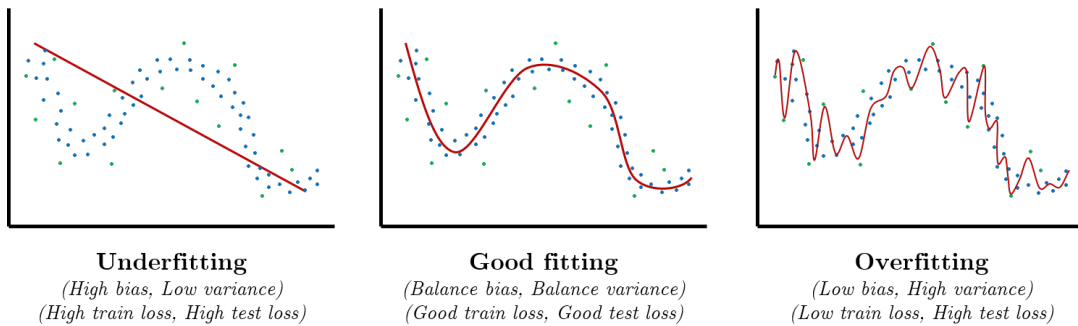

<div align="center">

Underfitting
(High bias, Low variance)
(High train loss, High test loss)

Good fitting
(Balance bias, Balance variance)
(Good train loss, Good test loss)

Overfitting
(Low bias, High variance)
(Low train loss, High test loss)

</div>

Fig. 15. The typical performances of the ANN model

Both underfitting and overfitting models should be modified and re-trained. There are numerous techniques to overcome these problems such as changing the architecture and optimizer hyperparameter, adopting the DL techniques, changing the type of the ML model, etc. In this study, the model performance was evaluated after the hyperparameter tuning process. For underfit problem, increasing the total parameter may be a good solution while several DL techniques can be adopted to prevent the overfitting problem.

5.3. Deep Learning techniques

As mentioned in the previous subsections, there are various of DL techniques that prevent the overfitting problem. Due to the high computational cost of FEM simulations, the dataset in this study consists of approximately 1800 samples of nine beam response. However, the dataset also includes noise data which is presented in the next section. Therefore, the model that trains on these data may not perform well on the test data. In this work, three techniques are adopted with different hyperparameter to solve this problem. These methods are the kfolds cross validation, the dropout technique, and the

early stopping conditions. The k-folds cross-validation is the data splitting technique where the dataset may be divided into k group and applied to k model. In each model, one of the data groups is used as the validation set while others are used in the train process.

Both dropout and early stopping techniques, however, do not affect the dataset. Dropout neural network is a neural network with several random nodes are deactivated in the train phase, this number of nodes is defined by the dropout rate. In contrast, all nodes are included in test phase but with a reduced loss value. The reduced rate is also equal to the dropout rate. This type of model is indicated to lessen the test loss value. On another hand, the early stopping technique only modified the stop condition of the train process. For instance, the stop may occur when the pre-defined minimum validation loss value is reached. The motivation of this technique is that with a longer training time, the model tends to fit the train dataset excessively (please see Fig. 16).

In this study, due to the small and noisy dataset, the typical ANN model may not produce good approximations for entire dataset. Consequently, the above techniques for handling overfitting were adopted. At first, the model is established with the kfolds cross validation of four along with the early stopping condition of minimum validation loss in several epochs. The trained model is assessed by six performance metrics. From this evaluation, methods to enhance the model performance are adopted. The final model is then conducted for further applications.
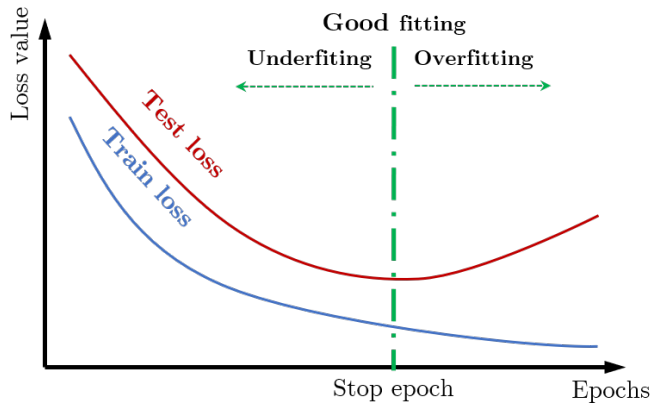

Fig. 16. The performance of the ANN model based on training epochs

6. RESULTS AND DISCUSSIONS

6.1. Finite element analysis results

6.1.1. *Convergence study*

The mesh size of 4 mm might be indicated as the relevant mesh for TPMS reinforced structures in previous studies [17]. However, due to the increment in number of layers, the unit size of the TPMS structure is reduced and the mesh size should be re-considered.

Therefore, another meshing strategy is implemented in this study that the TPMS unit is meshed with a certain number of elements to remain its smoothness which is illustrated in Fig 17. The molds and the cementitious core mesh size are constantly 4 mm. The meshing grid of the one-layer beam are given in Fig. 18.
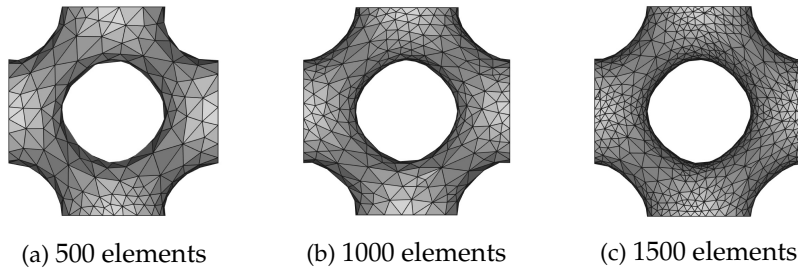

(a) 500 elements   (b) 1000 elements   (c) 1500 elements

Fig. 17. TPMS unit with different triangular mesh grids

(a) Plastic scaffolds

(b) Cement core
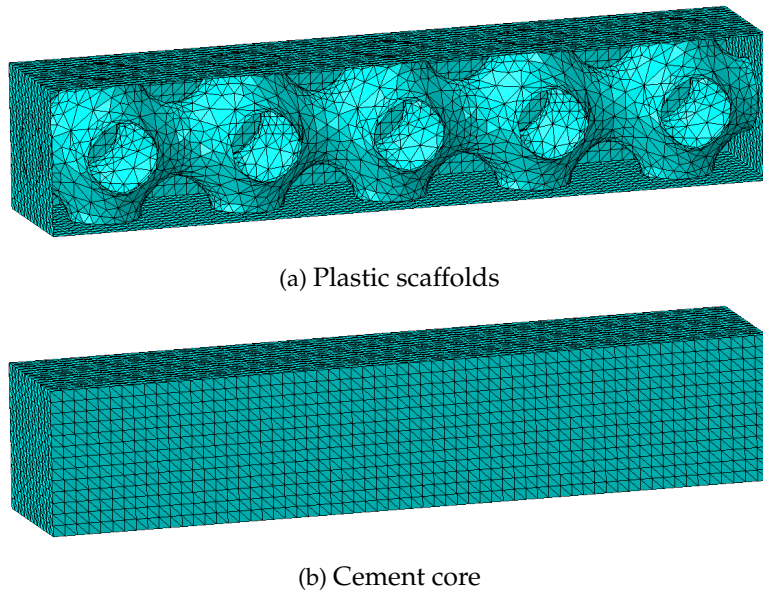
Fig. 18. The mesh grid of the one-layer beam with 1000 meshing elements for each TPMS unit

To conduct the most suitable number of mesh elements for each TPMS unit, all three mesh grids are adopted in the simulations. The convergence study of this mesh strategy is provided in Fig. 19 for beam PC1. As the result, the mesh grid of at least 1000 elements could produce a good solution. For reducing the computational time, this minimum-value element mesh is further used in this study. In addition, the FEM results conducted from this meshing grid are comparable with the experiments in the previous study [17]. The deviations of these results for beam PC1 and PC2 are 9.6%, and 10.7%, respectively. The force-displacement curves of these beams can be seen in Fig. 20.
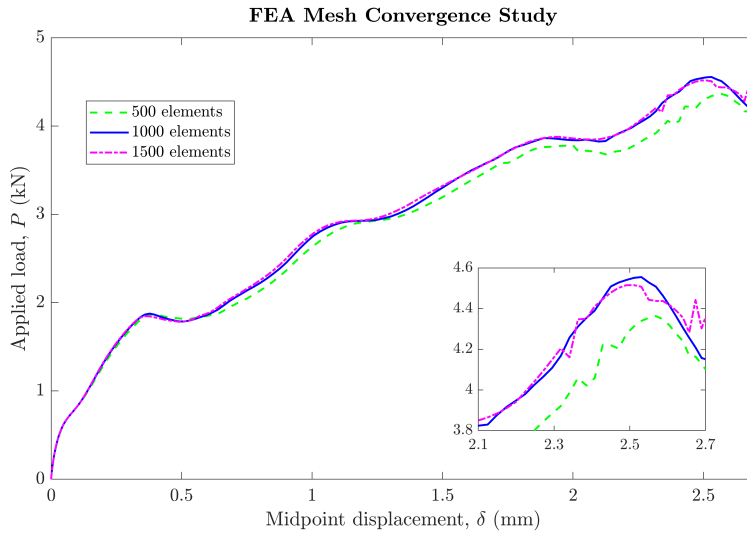
Fig. 19. The convergence study of PC1 beam for various numbers of meshing element for TPMS core
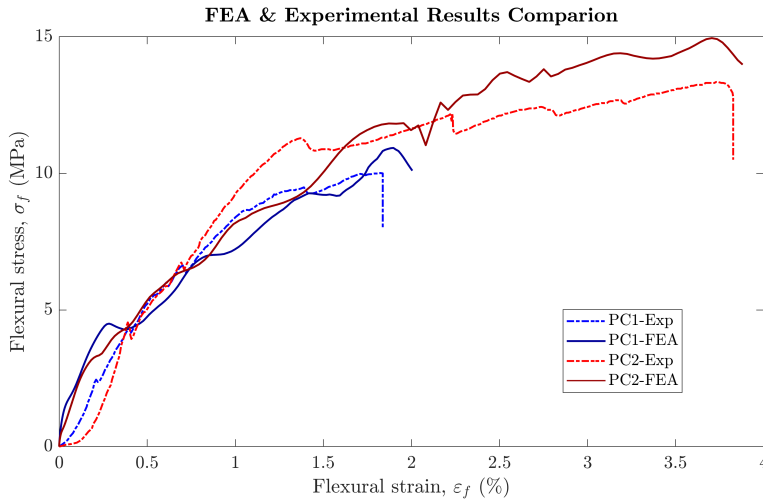

Fig. 20. Comparisons between FEM results in the present study and the experimental results in publication [17] of PC1 and PC2 beams

6.1.2. *Influences of TPMS properties*

By applying the proposed meshing method, the simulations of other beams are implemented. The stress distribution of the plastic components and the cement components of several beams are described in Fig. 21 and Fig. 22, respectively. These results well agree with the previous study with the view of stress distribution in the TPMS core. The higher value of TPMS layers may help the stress be more evenly distributed, especially at the
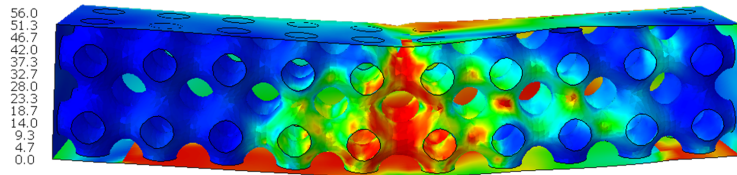
middle of the beam. The increment in the shell thickness may provide the similar result but with a smaller effect. It is suggested that in the odd-layer beam, the stress tends to concentrate at the gap between TPMS units, where the confinement is less than that at the center of the beam.
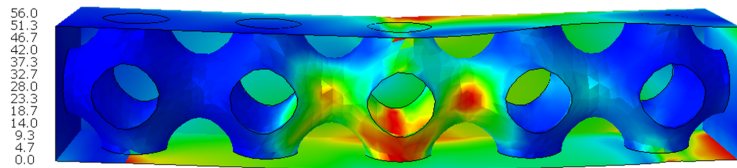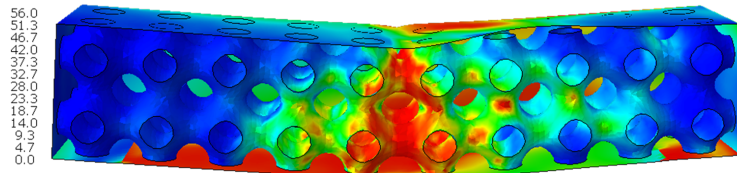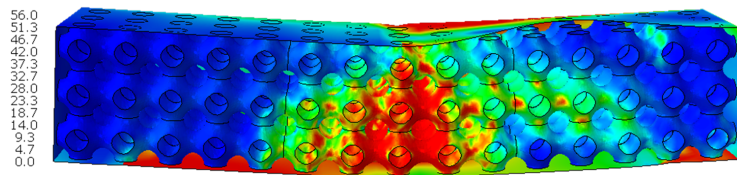

(a) Beam PC4
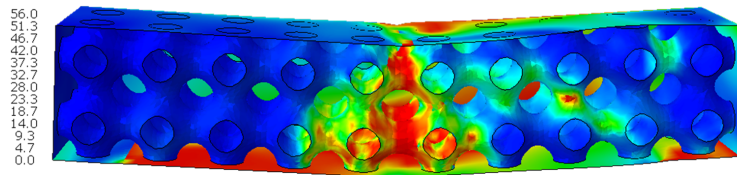
(b) Beam PC2

(c) Beam PC5
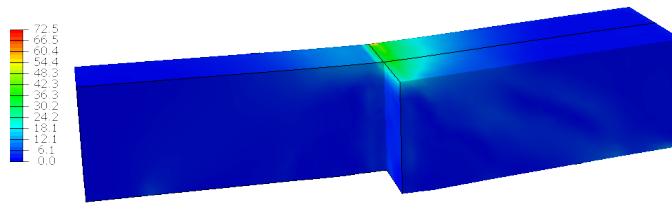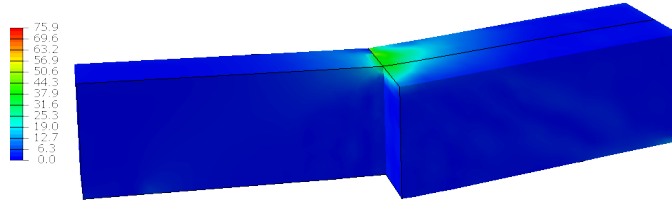

(d) Beam PC8

(e) Beam PC6

Fig. 21. The von Mises stress of plastic components

(a) Beam PC4

(b) Beam PC2
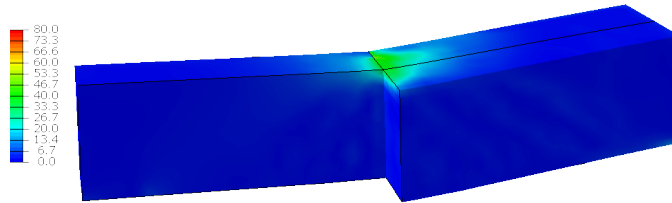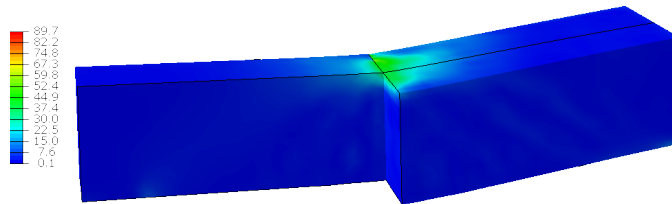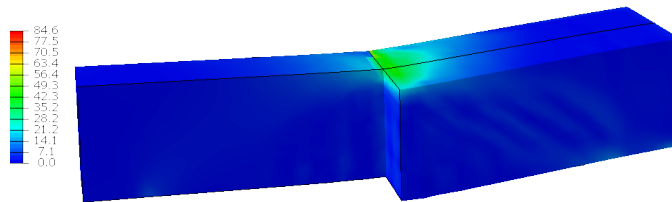

(c) Beam PC5

(d) Beam PC8

(e) Beam PC6

Fig. 22. The von Mises stress of cement components

In addition, both maximum and average von Mises stress at the load interaction lines of beam PC2 are comparable to the simulation in the previous study [17]. For instance,

the maximum stress in the previous study is about 82 MPa, while this value equals to 76 MPa in this study. Similarly, the average stress of the previous and the present studies are 45 MPa and 44 MPa, respectively. This slight disparity can be the result of the meshing strategy. Both the increments in TPMS layers and volume fraction lead to the improvement in the von Mises stress of the cement parts. On another hand, the effect of one-layer increment on the maximum cement stress may not outperform the contribution of 5% volume fraction in the two-layer beam. It is considered that as the thickness of the TPMS shell increase, the cement may be more confined.

(a) One-layer beam

(b) Two-layer beam

(c) Three-layer beam
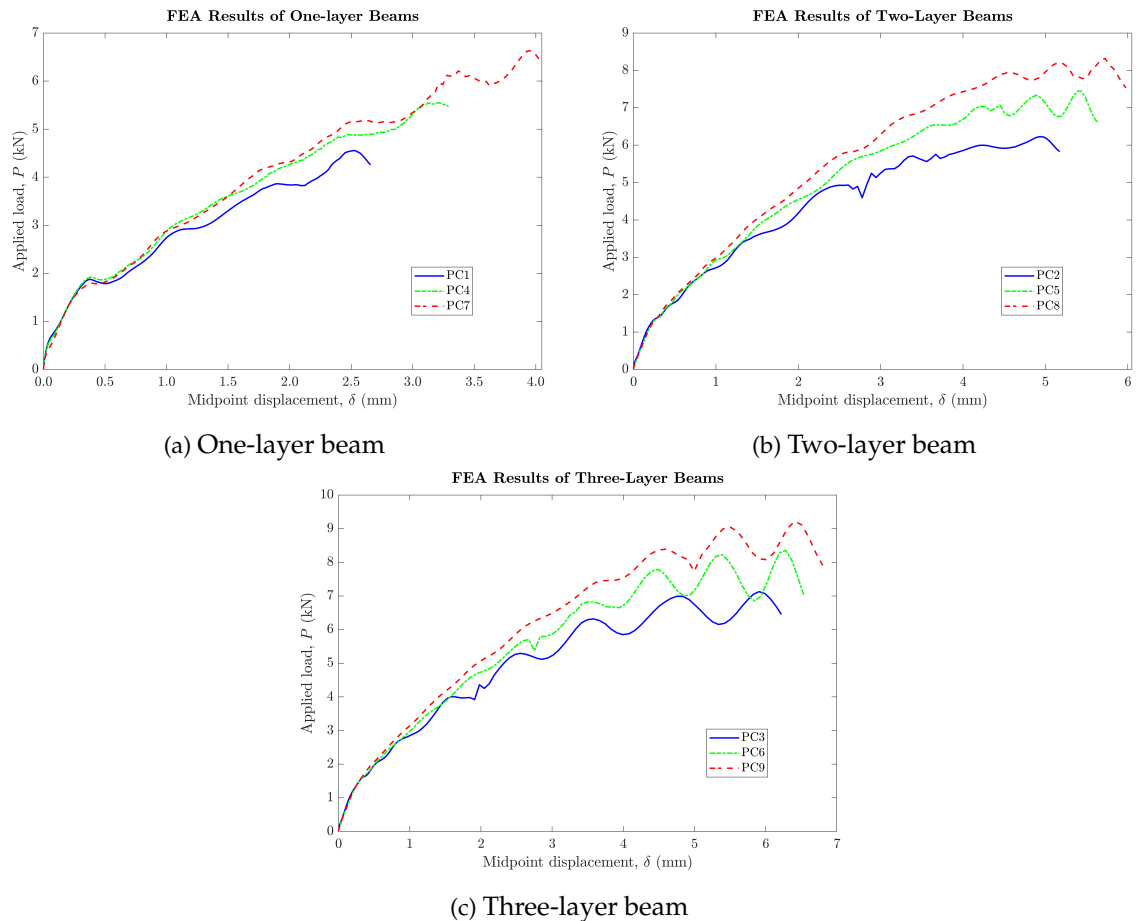
Fig. 23. The force – displacement curves of TPMS reinforced beams

In view of the force-displacement relationship, the simulation results are presented in Fig. 23. The peak loads and the maximum deflection of the investigating beams are provided in Table 7 where the values in the parentheses are the mean values of the oscillating curves. The maximum peak load of all nine cases is generated from beam PC9 with a value of 8.295 kN. It is observed that a higher volume fraction could provide more ductility and bending stiffness which is similar to the report [16]. For instance, the peak

loads of 15% and 20% volume fraction for one-layer beam has raised about 21% and 45%, 14% and 29% for two-layer beam, and 13% and 28% for three-layer beam, respectively. From this result, the higher-layer beam may provide a more stable peak load value. In another word, the increment in the volume fraction may be less effective when the number of TPMS layers reaches a certain value. The unique geometry of the TPMS can be considered the reason. The true mechanical properties of the TPMS structure can only be achieved with a specific number of layers. This theory was verified by numerous studies with both simulations and experiments. In fact, with at least 4 layers, the Primitive structure could receive its micromechanics properties including strength and elastic modulus [39]. A similar tendency can be found in the maximum midpoint displacement responses. Even with the double thickness, the three-layer beam can only increase about 7% in the maximum displacement.

Table 7. The peak load and the maximum deflection of nine TPMS reinforced beams based on FEA simulations

Volume fraction	Number of TPMS layers		
	1	2	3
	Peak Load (kN)		
10%	4.555	6.230	7.127 (6.623)
15%	5.546	7.448 (7.095)	8.356 (7.536)
20%	6.628	8.319 (8.013)	9.216 (8.580)
	Maximum displacement (mm)		
10%	2.531	4.982	5.986
15%	3.224	5.435	6.280
20%	3.973	5.724	6.406

On the other hand, as the number of TPMS layers increased, both the peak load and maximum deflection of the beam are improved. The amount of 37% is the average increment of the three-layer beam's peak load for all three volume fractions. The midpoint displacement, however, is improved with a greater average value of 98%. Consequently, it could be noted that the impact of TPMS layers on the deflection is greater than on the maximum load. Further discussions on this tendency are included in the next section with various non-computed schemes. Moreover, due to the nonlinearity behavior of the material, the force-displacement curves of three-layer beams are confusing and are not smooth. To specify the correct value of the fit curve might need to be included. In this case, the ML surrogate model is possibly a good approximation model not only for one specific case but also for all train cases. The final result of the next section can verify this presumption.

6.2. Machine learning surrogate model results

In this subsection, the most suitable surrogate model is conducted based on the ANN model with the support of DL techniques. It is suggested in Section 5 that the small FEA

dataset of TPMS beams may cause the model to be overfitting. Therefore, a three-phase process is implemented to search for the best model. This process consists of the initial model hyperparameter tuning, the model assessment, and the handling overfitting phase. A sequential diagram of this process is given in Fig. 24 where the data and techniques used in each process are listed in the following Table 8 and Table 9, respectively.
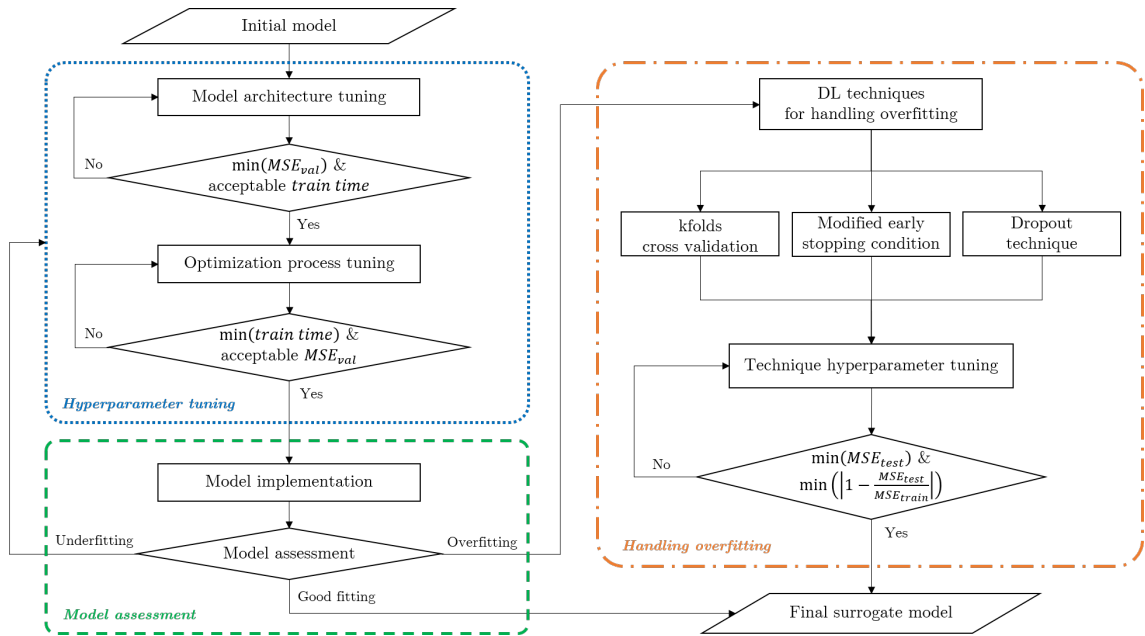
Fig. 24. The process of finding the most suitable surrogate model

Table 8. The dataset used in the process of finding the final surrogate model

Volume fraction	Dataset		
	Train	Validation	Test
Model hyperparameter tuning	PC1 ÷ PC5	PC1 ÷ PC5	
Model assessment	PC1 ÷ PC8	PC9	PC9
kfolds cross validation tuning	PC1 ÷ PC8	PC9	PC9
Dropout tuning	PC1 ÷ PC8	PC9	PC9
Modified early stopping condition tuning	PC1 ÷ PC8	PC9	PC9

It should be noted that all the ANN model are conducted with a personal computer in Python 3.8 languages with the support from TensorFlow and scikit-learn opensoured libraries. The configuration of this computer is 4 processors of Intel Core i7U, CPU 2.7GHz, 16GB memory, and WindowOS.

Table 9. The modified properties of the model used in the process of finding
the final surrogate model

Volume fraction	The modified properties		
	Stop condition	Number of kfolds	Dropout rate
Model hyperparameter tuning	$\min\left(MSE_{val}\right)$	4	
Model assessment	$\min\left(MSE_{val}\right)$	4	
kfolds cross validation tuning	$\min\left(MSE_{val}\right)$	2; 3; ...; 10	
Dropout tuning	$\min\left(MSE_{val}\right)$		0; 0.1; ...; 0.8
Modified early stopping	$\min\left(MSE_{val}\right);$		
condition tuning	$\min\left(\left\|1 - \dfrac{MSE_{test}}{MSE_{train}}\right\|\right)$		

6.2.1. *Model hyperparameter tuning*

In this process, the ANN model hyperparameters is noted to strongly affect the overall performance of the model. These hyperparameters might be split into two main group that are the architecture group and the optimizer group. At first, the impact of model architecture is investigated with various combinations of number of layers, number of nodes, and activation function. These combinations are presented in Table 10 along with two optimizers and three different stop patience values. In addition, it is noteworthy that the output layer's activation function is the 'SoftPlus' function for all cases due to the necessity of the smooth output range being $[0, +\infty)$.

Table 10. Hyperparameters sets adopted in the architecture tuning process

Hyperparameter	Values
Number of hidden layers	2; 3
Number of nodes-per-layer	50; 100; 150
Hidden layers activation function	'ReLU'; 'SoftPlus'; 'Sigmoid'
Optimizer	'Adam'; 'SGD'
Learning rate	0.005
Batch size	32
Stop patience	10; 20; 30

Furthermore, it should be noted that the optimizer parameters are crucial factors in the training process of an ANN model, especially the learning rate. This hyperparameter is later investigated along with the batch size and the stop condition value. In this study, other hyperparameters of the optimizer are adopted as the default value in the Keras library. The only exception is the momentum value of the 'SGD' optimizer, which is changed into the value of 0.9. As mentioned above, the data samples from PC1 to PC5 are used to train the model in this process. In this process, the kfolds cross validation of four divided the data into 4 train-validate sets and the model metrics are calculated by

the average values of all folds. Additionally, the stop condition is based on the minimum value of the validation loss function. The train process stops when the loss value cannot decrease for the last several epochs, which is called the stop patience value. The model weights and bias are collected at the stop epoch which provide the smallest loss value. By employing the above training strategy for hyperparameter tuning, approximately 650 models have been conducted. The evaluation metrics for these models consist of the total parameters, the validation loss (MSE_{val}), and the training time. Moreover, for a comprehensive evaluation, the average value of three times training is adopted. It should be noted that due to the random initialization of model weights and bias, the performance of a model can be varied. In other words, the model with a higher number of total parameters may produce a less efficient result compared with other models being less complexity. However, by conducting the assessment through the average metric of several run times, the influence tendency of a hyperparameter can be obtained.

Table 11. The first three best models for loss value with 'Adam' optimizer

ID	Architecture	Total parameters	Activation function	Stop patience	MSE_{val} (kN^2)	$RMSE_{val}$ (kN)	MAE_{val} (kN)	Training time (s)
#643	(150,150,150)	46051	'ReLU'	30	0.0066	0.0870	0.0595	41.7
#511	(050,100,100)	15501	'ReLU'	30	0.0067	0.0795	0.0547	67.1
#619	(150,100,100)	25901	'ReLU'	30	0.0069	0.0827	0.0557	54.3

Table 12. The first three best models for computational time with loss value less than 0.01 and 'Adam' optimizer

ID	Architecture	Total parameters	Activation function	Stop patience	MSE_{val} (kN^2)	$RMSE_{val}$ (kN)	MAE_{val} (kN)	Training time (s)
#367	(100,150,100)	30751	'ReLU'	20	0.0093	0.0960	0.0652	35.3
#421	(150,150,100)	38451	'ReLU'	20	0.0099	0.0987	0.0680	39.6
#496	(100,100,050)	15601	'ReLU'	30	0.0085	0.0921	0.0644	40.5

The results indicate that the 'Adam' optimizer is more effective than the 'SGD' one, which has been reported in numerous studies. Therefore, the three best models for loss value and computation time with a minimum loss value of 0.01 are shown in Table 11 and Table 12, respectively. These results are generated by the 'Adam' optimizer. Moreover, the stop patience value of 30 can help the model find a better solution. Both impacts of different optimizers and stop patience values on the model performance are revealed in the next step. The validation loss and the training time of the proposed architectures with 'Adam' optimizer and stop patience of 30 epochs are described in Fig. 25 along with a linear fit curve for each activation function data. In Fig. 25, the 'ReLU' function might be noted as the dominant activation in this model. It is probable that the output range of $(0, +\infty)$ and the step point at 0 can reduce the objective function value in gradient descent optimization algorithms even with lower epochs. Moreover, the metrics of the

three first best models in Table 11 have shown that as the complexity of the model increase, higher accuracy may be achieved during the train process. This affirmation has also been proven with the linear fit curves in the above figure. The model with a higher number of total parameters can provide better results with less computational time due to the early stopping condition. Consequently, the final model for further investigation is model number #643 which might give the minimum loss value in this architecture tuning process along with an acceptable training time of 41.7 s.
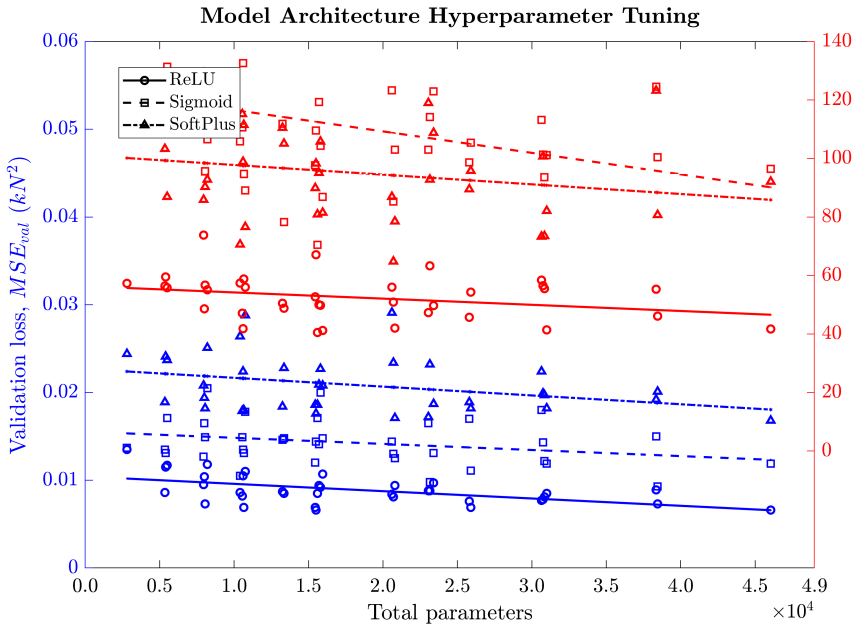

Fig. 25. Loss values and computation times of various architectures and activation functions ('Adam' optimizer and stop patience value of 30)

Next, the optimization hyperparameter tuning process is conducted, where the best architecture concluded above is adopted with various optimizers. Similar to the previous tuning process, the average values of 10 train times are used to evaluate the results. In this process, the tunable parameters are the optimizer, the learning rate, the batch size, and the stop patience with different values from the previous tuning process. The values of these parameters are given in Table 13.

At first, the influence of the stop patience is demonstrated in Table 14 and Table 15 for validation loss and training time, respectively. The results show that a lower loss can be obtained with the higher stop patience, but it may cost a longer training time. For instance, the loss value of the 'Adam' optimizer reduces only 20% for both learning rates but its training time increases by 50% and 37% for the learning rate of 0.005 and 0.01, respectively. In addition, the stop patience value of at least 30 epochs should be used due to the fact that the lost values of the 10-epoch stop patience are much higher than others. With the 30-epoch stop patience, the loss values have decreased by 73%, 66%, and 81%

Table 13. Hyperparameter sets adopted in the optimization tuning process

Hyperparameter	Values
Model architecture	(150,150,150)
Hidden layers activation function	'ReLU'; 'SoftPlus'; 'Sigmoid'
Optimizer	'Adam'; 'SGD'; 'RMSprop'
Learning rate	0.005; 0.01
Batch size	16; 32; 64; 128
Stop patience	10; 30; 50

Table 14. The validation loss MSE_{val} (kN^2) of various optimizers and stop patience values

Volume fraction	Optimizer					
	'Adam'		'SGD'		'RMSprop'	
	0.005	0.010	0.005	0.010	0.005	0.010
10	0.0335	0.0402	0.5871	0.5933	0.0875	0.1473
30	0.0088	0.0109	0.1732	0.2308	0.0181	0.0260
50	0.0069	0.0087	0.0542	0.0719	0.0122	0.0184

Table 15. The training time (s) of various optimizers and stop patience values

Volume fraction	Optimizer					
	'Adam'		'SGD'		'RMSprop'	
	0.005	0.010	0.005	0.010	0.005	0.010
10	32.1	26.1	024.2	020.0	34.2	28.6
30	48.2	47.9	073.7	062.1	62.3	55.2
50	72.4	65.5	105.8	114.9	84.4	78.7

for the 'Adam', 'SGD', and 'RMSprop', respectively. Besides, the impact of this parameter on the 'SGD' loss value might be greater than that of other optimizers. This feature can be explained by the non-adaptive learning rate of the 'SGD' optimizer which is constant during the train process. This optimizer may also need more time to provide comparable results to 'Adam' and 'RMSprop' optimizers.

in the next step, the batch size of the model is revealed with different optimizers and learning rates as shown in Fig. 26. The 'Adam' optimizer with a learning rate of 0.005 might be the most suitable solution for the present problem. By increasing the batch size, the model can achieve higher accuracy yet have greater training time for adaptive optimizers namely 'Adam' and 'RMSprop'. Each epoch may be accomplished faster with the high value of batch size but the model may need more epochs to receive the convergence

result. In addition, the learning rate of 0.005 could outperform the learning rate of 0.01 for all three optimizers in view of loss value. In contrast, the computational times of the higher learning rate are almost always shorter. Due to the purpose of finding the appropriate optimizer hyperparameters that have the ability to produce both good results and short training time, the 'Adam' optimization algorithm with a learning rate of 0.005 and batch size of 32 is utilized for further investigations.
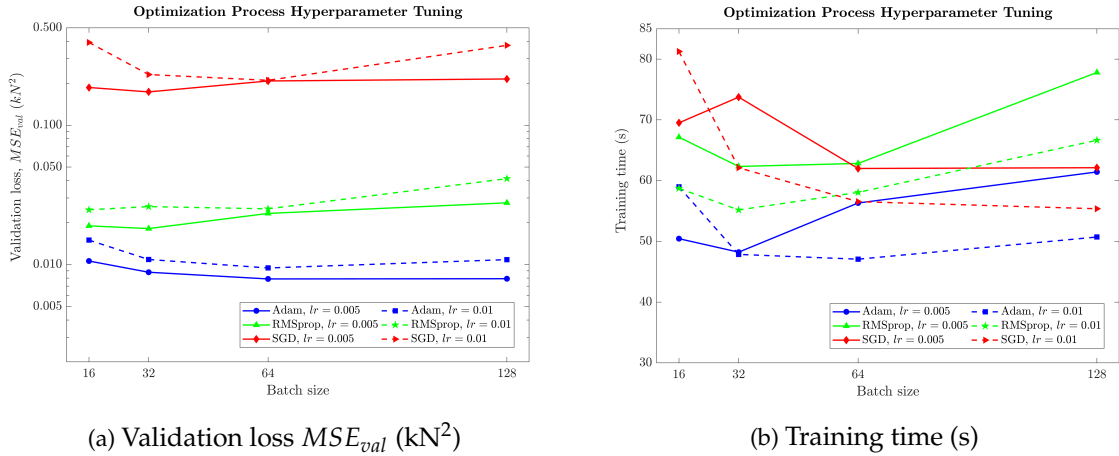

(a) Validation loss MSE_{val} (kN^2)   (b) Training time (s)

Fig. 26. The validation loss and training time of various optimizers and batch size values

6.2.2. *Model assessment*

In this process, the most effective hyperparameters conducted from the previous subsection are adopted to establish a new model. This model had the architecture of model number #643 and is computed by the 'Adam' optimizer with the setup conducted in the previous subsection. To assess this model, six performance metrics are provided that are focused on the results of the test process. In these metrics, the correlation loss of train and test data is introduced to determine the overfitting effect. The higher value of these metrics may indicate the more overfitting model is. The metrics of the new model are shown in Table 16. The value of test loss is five-time higher than the train loss, which is given in the correlation metrics of 4.8553. The convergence history of a typical fold shown in Fig. 27 indicates a similar result. From these evidences, this model can be considered as overfitting.

Table 16. Performance metrics of the hyperparameter tuned model

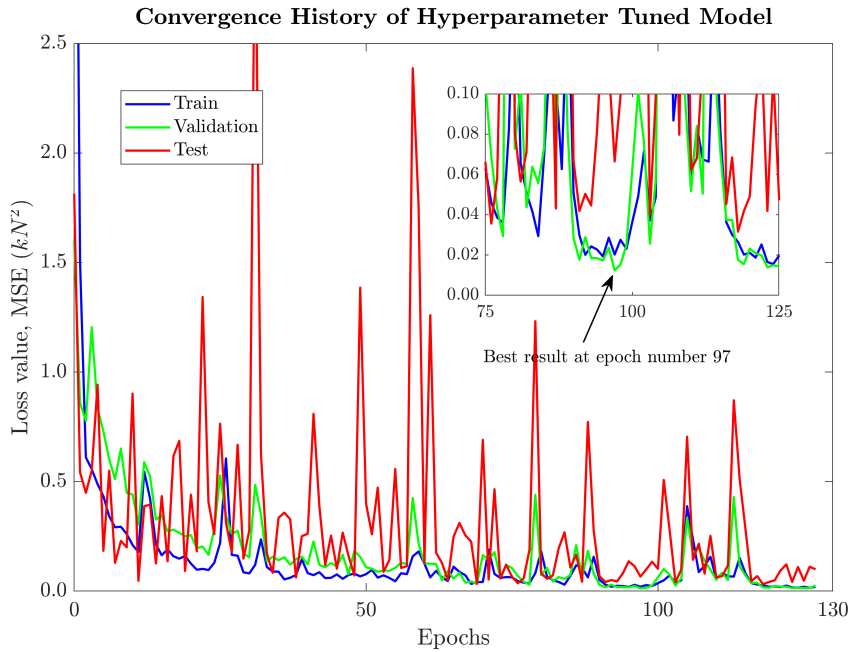| MSE_{train} (kN^2)	MSE_{test} (kN^2)	$\left(\left\| 1 - \dfrac{MSE_{test}}{MSE_{train}} \right\| \right)$	$RMSE_{test}$ (kN)	MAE_{test} (kN)	Training time (s)
0.0152	0.0738	4.8553	0.2656	0.1963	50.8

Fig. 27. Convergence history of the hyperparameter tuned model.

6.2.3. *Handling overfitting*

In this study, three types of techniques are employed to handle the overfitting problem. The impact of the key hyperparameter of each technique is investigated on the model performance. It is noted that the model architecture and optimizer are adopted from the previous hyperparameter tuning process. The mean results of ten technique tuning processes are provided in Fig. 28. Since the number of folds reaches 5, the test loss values are steady at 0.05 and cannot have an obvious decrease. However, the training time increases proportionally with the number of folds. Another linear relationship that can be noted is the impact of the stop patience value on the training time of the modified stopping condition models. In contrast, the dropout rate may create a smaller effect on the training time. By applying the dropout rate of 0.1 to 0.3, the loss value of the test set may have a slight reduction. The results in Fig. 28(c) show that the performance of the model is slowly enhanced with the increase of stop patience.

For comparisons of different methods, the model that has the best result in the loss value of each method is adopted. These models are the 8-kfolds model, the dropout model with the dropout rate of 0.1, and the modified early stopping condition with 300 patients. The assessment metrics consist of the six performance metrics proposed in subsection 6.2.2. In this subsection, however, these metrics are normalized with the smallest value of three techniques as follows

$$A_i = \frac{metric_i}{\min\left(metric_i\right)} \tag{20}$$

where A_i are the normalized performance values; $metric_i$ are the performance values; i are the metric types, $i = MSE_{train}; MSE_{test}; \left(\left| 1 - \dfrac{MSE_{test}}{MSE_{train}} \right| \right); RMSE_{test}; MAE_{test}$; training time.

(a) kfolds cross validation

(b) Dropout technique

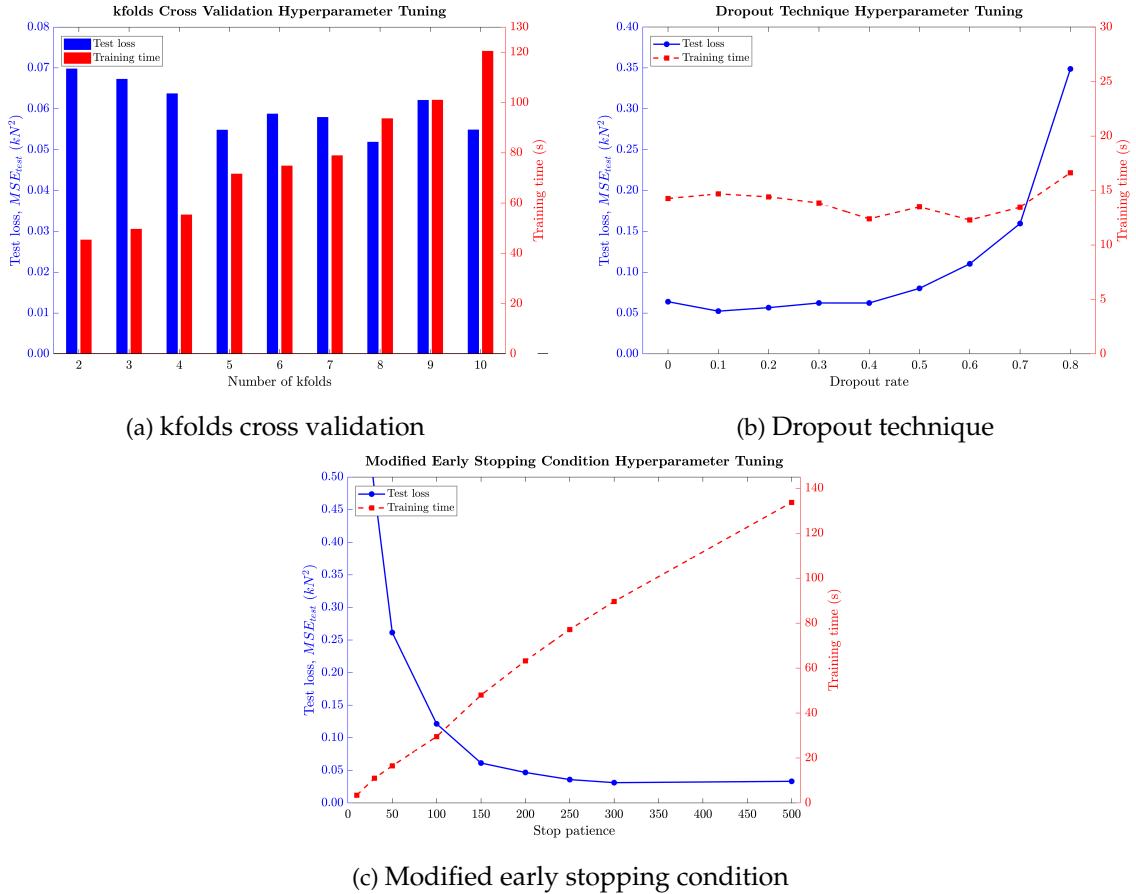(c) Modified early stopping condition

Fig. 28. The impacts of various Deep Learning techniques on the on the test loss MSE_{test} and the training time.

For average results in Fig. 29, the modified early stopping model has the best performance on the test loss and metrics. This technique also has a comparable train-test loss correlation to the dropout technique. Although the dropout model shows great performances in both time and test loss aspects, the train loss value of this model is much smaller than other models. Similarly, the kfolds model can produce the best result in train loss yet failed to predict new data on the test set. In contrast, the train loss performance value $A_{MSE_{train}}$ of the early stopping model could reach 79% the maximum value of all three models. This rate is about 94% for the case of best-test-loss models. It should be noted that there might be an epoch result that had good loss values of both train and test data in Fig. 27. This affirmation could be seen as the reason for employing the correlation

of the losses as a stop condition. In brief, the above tuning results and comparison results indicate that the modified early stopping model with stop patience of 300 epochs is the most efficient model for this study problem.
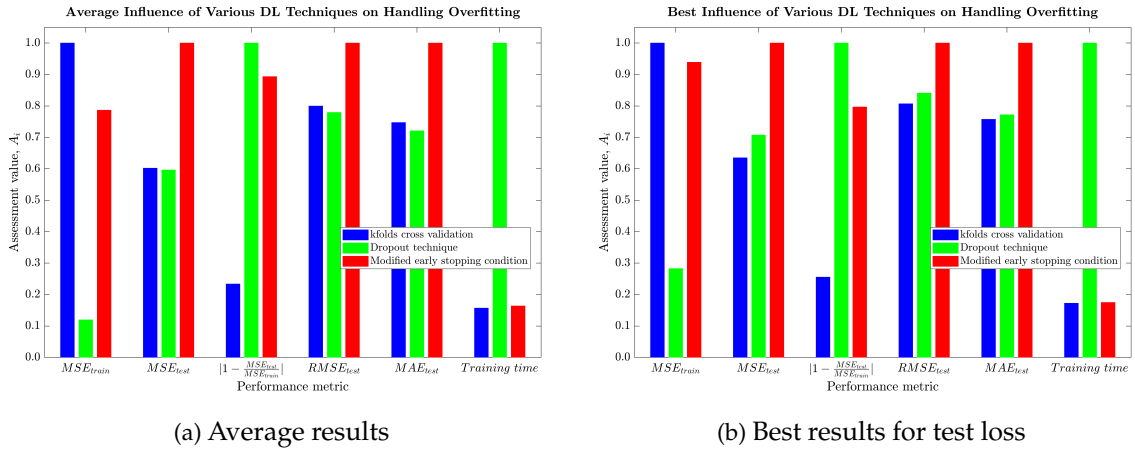

(a) Average results (b) Best results for test loss

Fig. 29. The influence of different DL techniques on handling overfitting.
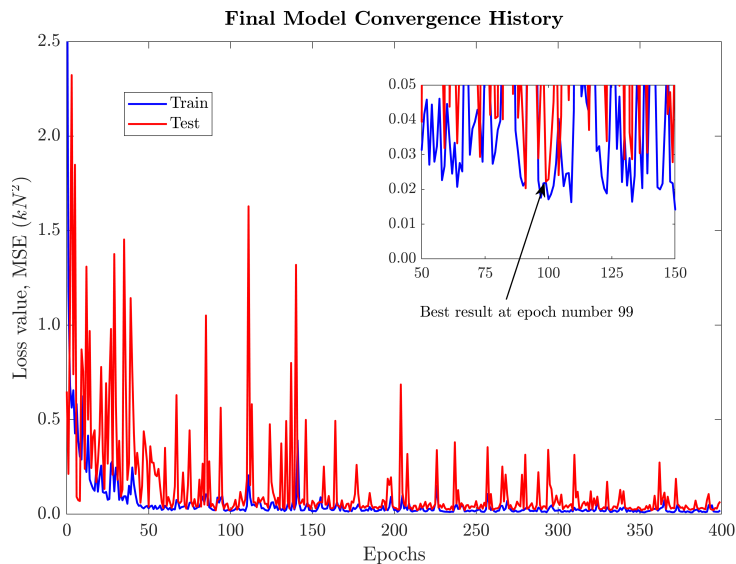

Fig. 30. Convergence history of the final model

The convergence history of this model is presented in Fig. 30. At epoch number 99, both loss values of train and test data are minimized. It is noted that during the training process, a smaller value of train loss could be obtained but the test loss may be slightly higher. For deeper analysis, the performance metrics of this model are provided

in Table 17. The results show that the correlation index of the present model is 10.3 times smaller than the previous one. The test loss has also been remarkably reduced to 1/3 the earlier value. Besides, the train loss is slightly lessened due to the high value of stop patience. Another impact of the high stop patience is the greater training time. Although the response of beam PC9 was not included in training the model, good approximations can be generated from the final model with the average absolute error of the applied load at all points being only about 0.1 kN along with the average root mean square error of 0.15 kN.

Table 17. Performance metrics of the final model.

MSE_{train} (kN^2)	MSE_{test} (kN^2)	$\left(\left\|1 - \dfrac{MSE_{test}}{MSE_{train}}\right\|\right)$	$RMSE_{test}$ (kN)	MAE_{test} (kN)	Training time (s)
0.0151	0.0222	0.4698	0.1491	0.0953	89.1

6.2.4. *Final model predictions*

Applying the above well-trained model, the force-displacement curves of nine investigating beams could be generated without FEA simulations as shown in Fig. 31. Furthermore, the computational time for all nine beams was only about 0.806s. The simulation calculation time of each beam varied from 266s for beam PC1 to 7600s for beam PC9. The ML model should be considered an excellent approximation for this study problem. The results of this model can work as valuable fit curves for the beams' responses, especially for the beam with noisy data. In addition, the smoothness of these fit curves is the result of the 'SoftPlus' activation function at the output layer. Moreover, this model can be used to predict the behaviors of different TPMS reinforced beams. The peak loads and the maximum midpoint displacements of these new beams are adopted to formulate the peak load surface and the maximum displacement surface. The word 'surface' indicates the impact of both volume fraction and number of TPMS layers on the corresponding feature. These surfaces are demonstrated in Fig. 32 and Fig. 33 for peak load and maximum deflection values, respectively. In these graphs, the FEA results are denoted as the black points. The peak load and deflection of the non-reinforced beam are adopted from the previous study [17], which were 2.88kN and 1.35mm, respectively.

It could be noted that there are well agreements between the peak loads from both approaches with the largest deviation being 2.5%. The impact of volume fraction on the beam peak load in each number of reinforcement layers can be described as a linear relationship. From the peak load surface projection, these lines are possibly parallel to each other but with different distances. While the step of about 1.5 kN is the variance between the one and two-layer beam peak load, the value of two and three-layer beams is only about 1 kN and reduce with the increment in the volume fraction. However, the predicted results of four-layer beams show the increase of peak load is strongly lessened at high values of volume fraction. In fact, the increment in peak load from three-layer to four-layer beams is only about 0.5 kN when the volume fraction is 20%. Consequently, the peak load curves of different numbers of layers with a certain volume fraction are
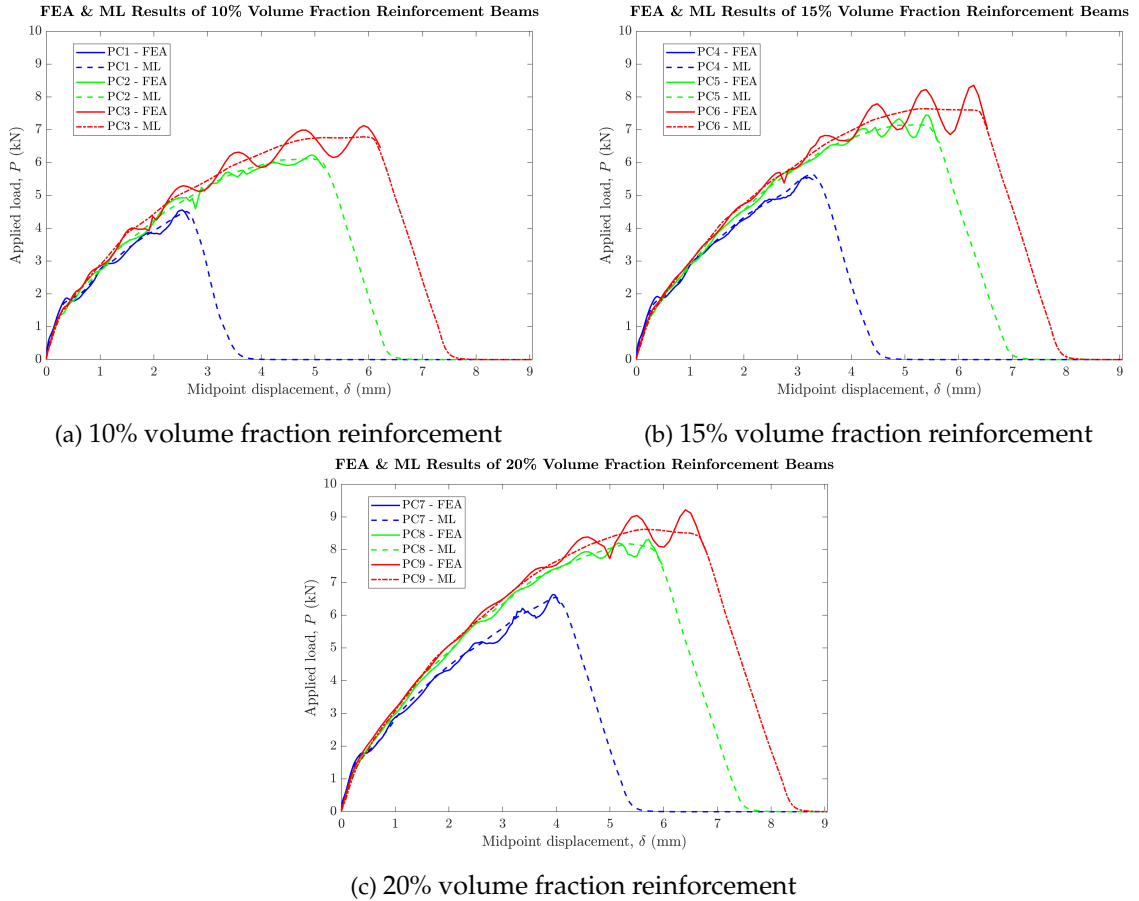
(a) 10% volume fraction reinforcement

(b) 15% volume fraction reinforcement

(c) 20% volume fraction reinforcement

Fig. 31. The force-displacement curves of various beams from FEA simulations and ML surrogate model

nonlinear. As the volume fraction increase, the corresponding curve tends to reach its maximum value only with a lower number of TPMS layers. In contrast, the 5% volume fraction TPMS reinforced beam has a relatively linear relationship between the peak load and the number of TPMS layers in the range of one-layer to four-layer reinforcement strategies. Generally, by increasing the number of layers, the peak load of the considering beams tends to attain a specific value. This value may be achieved with at least 4 layers of Primitive TPMS in case of 20% volume fraction, which is similar to the plastic TPMS beam in the research [39].

In the view of maximum deflection, the agreement between FEA and ML model can be again verified. The results show that the greatest deviation belongs to beam PC9 data with a value of 3.5%. Besides, the influence's tendencies on the deflection are also similar to peak load ones. However, the linear relationships between the volume fraction and the deflection of different TPMS beams are not parallel. For instance, the increasing pace in maximum displacement of one-layer beam to two-layer beam is greater at a lower
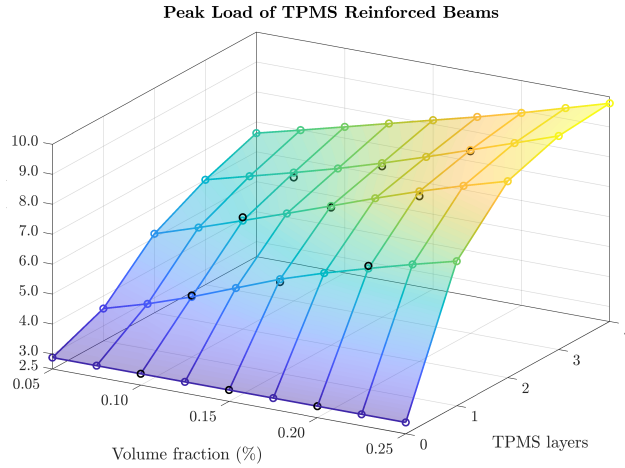
Peak Load of TPMS Reinforced Beams

(a) Overall view
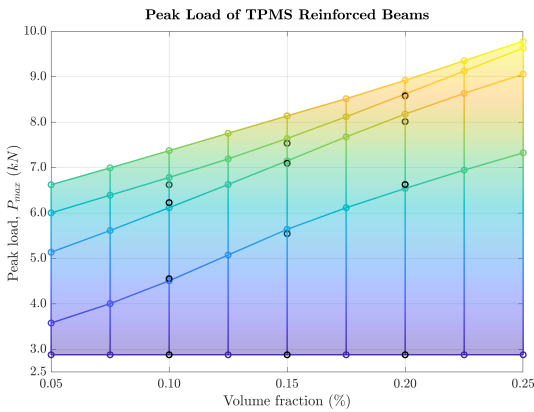
(b) Influence of the volume fraction
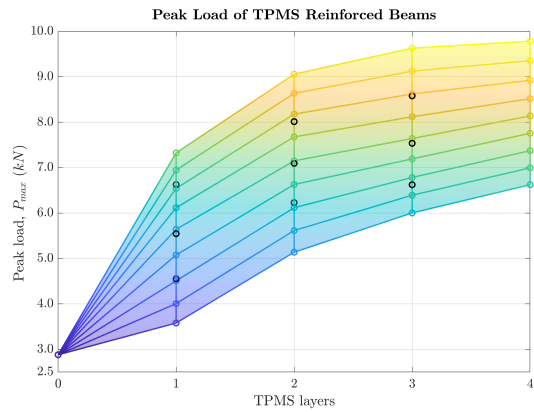
(c) Influence of the number of TPMS layers

Fig. 32. The predicted peak loads of the final surrogate model

volume fraction. This pace of a two to three-layer beam may be constant despite any value of the volume fraction which is also similar to the pace of a three to four-layer beam. Another similarity is the shape of relationship curves between considering property and the number of TPMS layers. It is observed that these correlations are nonlinear curves.

Due to the tiny deviations between the maximum displacements of two-layer and three-layer beams, the surrogate model might not generate the best predictions for this type of beam's response index. The deflections obtained from FEA simulations show similar tendencies as the peak load. It could be noted that there might be a displacement value that may not be exceeded only by increasing the number of core layers. In other words, by increasing the TPMS layers, the maximum displacement of the beam tends to reach a ceiling value. However, with a small value of volume fraction, increasing the number of layers might be more effective. The TPMS core shell may be too thin in the
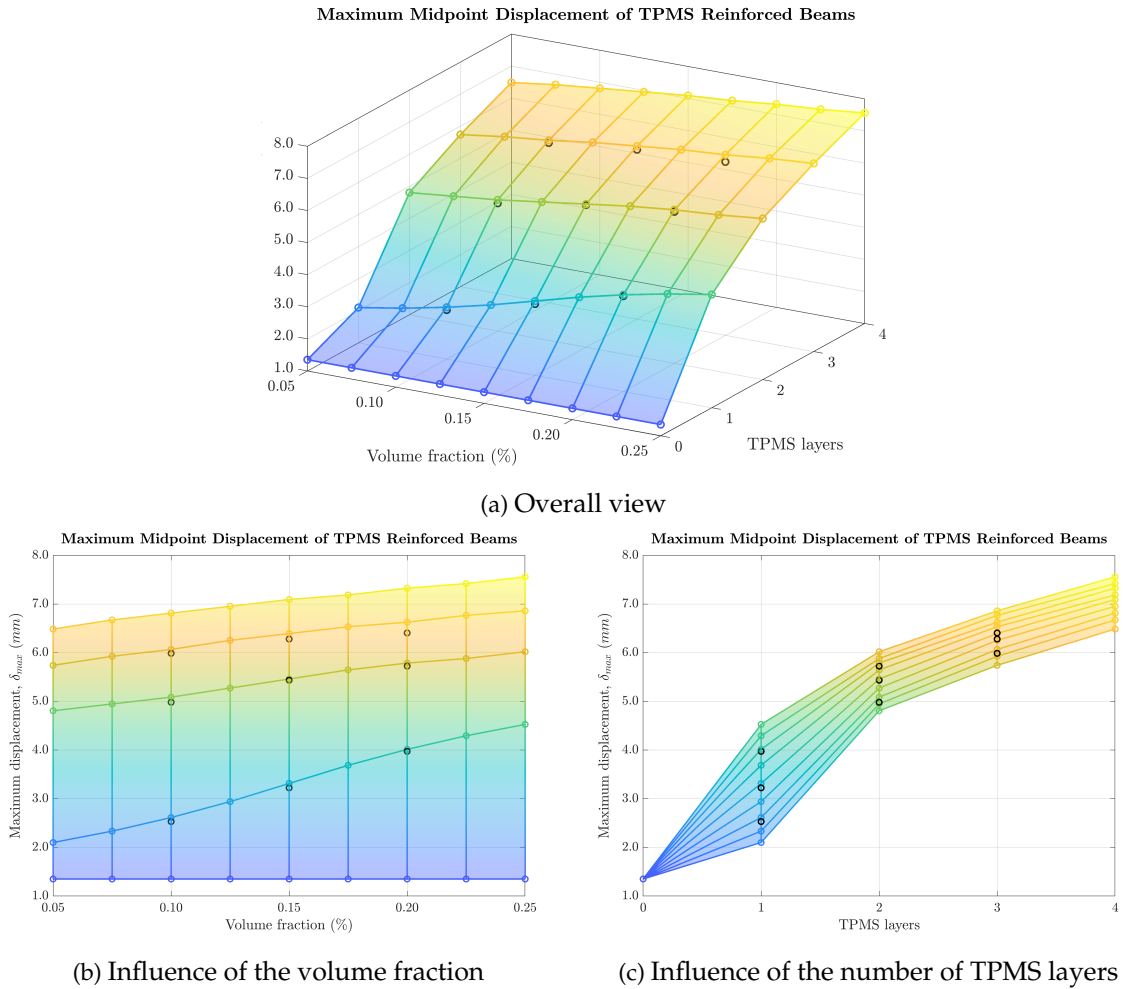
Maximum Midpoint Displacement of TPMS Reinforced Beams

(a) Overall view

(b) Influence of the volume fraction

(c) Influence of the number of TPMS layers

Fig. 33. The predicted maximum displacement of the final surrogate model

low-volume-fraction beams, and the strength of the beam might mainly depend on the strength of the cement core. With a greater number of layers in the beam, more cement confinement area could be produced and therefore increase the strength of the cement. This relationship was straightforward and could be described as linear function as in Fig. 32(c) and Fig. 33(c).

In sum, a higher number of TPMS layers could produce improved load-bearing responses for beam structures with both peak load and maximum deflection. However, fabrication difficulties should be noticed attentively. In fact, the core shell with *n* layers is *n*-times thinner than the single-layer one which is indicated in Eq. (8). Furthermore, one-layer beams can provide a comparable peak load with a higher value of the volume fraction. Nonetheless, it is suggested from Fig. 31 that a one-layer beam may have larger deflection than multiple-layer beams at the same load. This behavior can be reduced by

increasing the number of TPMS layers. For example, the force-displacement curves of both two and three-layer beams are close to each other. The complex geometry of the TPMS structure should be indicated as the key reason.

7. CONCLUSIONS

In this study, several Primitive TPMS reinforced beams including one, two and three core layers with three values of volume fraction have been investigated numerically. The response data of these beams were adopted to create an ML-based surrogate model with the support of ANN and DL features. Several remarks can be listed as follows

- New meshing strategy for the complex geometry of TPMS structures was proposed. This mesh based on the number of mesh elements was validated by experimental results in the previous study;
- Linear relationships between the volume fraction and the peak load of the beams could be denoted. The influence tendency of this aspect on the maximum deflection is similar but with a different slope for each number of TPMS layers;
- The impacts on both peak load and maximum displacement of the number of layers are nonlinear curves. With the increase of this number, the beam mechanical properties tend to reach ceiling values;
- Despite the noisy dataset, an ANN model with three 150-node layers, 'ReLU' activation function, 'Adam' optimizer, and early stopping condition of minimum validation loss could generate good results on the train dataset;
- Three DL techniques including the kfolds cross-validation, dropout, and modified early stopping conditions were employed to solve the overfitting problem in this study;
- Among all, the model with stopping condition of loss correlation should be noticed as the most suitable model for the present problem;
- The surfaces of peak load and maximum deflection were produced by the surrogate model to demonstrate the impact of both aspects of the TPMS core.

In sum, a well-trained surrogate model has been achieved. This model could produce excellent predictions for various reinforcement cases without inefficient FEA simulations. From this finding, the plastic TPMS reinforced beam can be directly modified to adapt to the requirements of numerous practical applications.

It should be noted that this study target is the Primitive TPMS which is only one of numerous TPMS structures that could be found. In fact, previous studies have investigated other types of TPMS structures including Gyroid, Diamond, IWP, Fischer-Koch, etc. Therefore, adopting these geometries in various concrete structures could be indicated as an interesting future direction. Besides, crack patterns, dynamic responses, and responses under various boundary conditions, etc, might also need to be revealed. Dominantly, the latest research of theoretical solutions for these TPMSs [15] is considered a promising approach to study on these complex structures. In fact, by combining the proposed theory from the mentioned work and the composite behavior theory, a full investigation of the considering beam responses can be conducted more efficiently.

In the view of creating surrogate models, there are various parameters of this beam that were not included in the present study. These parameters consist of beam size, bending test span, TPMS type, unit arrangement, etc. By adopting entirely tunable parameters of the beam, a completely general surrogate model can be created. However, the dataset used for this model could be extremely large. The proposed deep learning techniques in this study might not be suitable. To conduct good approximations, different techniques should be implemented. One of the remarkable solutions is enhancing the gradient descent algorithm with Sequential Motion Optimization as in the study of Leduc et al. [40]. By employing the sequential motion chain, the effectiveness of this model on the large data optimization problem has been verified. Different types of ML models should also be noted as alternatives including support vector machine (SVM), random forest regression, extreme gradient boosting (XGBoost), and unsupervised or reinforcement learning algorithms. Furthermore, the emerging physics-informed neural networks (PINN) model might be a potential approach to solve the present problem without the need of simulation results [41].

DECLARATION OF COMPETING INTEREST

The authors declare that they have no known competing financial interests or personal relationships that could have appeared to influence the work reported in this paper.

ACKNOWLEDGMENTS

REFERENCES

[1] B. Salazar, P. Aghdasi, I. D. Williams, C. P. Ostertag, and H. K. Taylor. Polymer lattice-reinforcement for enhancing ductility of concrete. *Materials & Design*, **196**, (2020). https://doi.org/10.1016/j.matdes.2020.109184.

[2] Y. Xu, H. Zhang, Y. Gan, and B. Šavija. Cementitious composites reinforced with 3D printed functionally graded polymeric lattice structures: Experiments and modelling. *Additive Manufacturing*, **39**, (2021). https://doi.org/10.1016/j.addma.2021.101887.

[3] N. S. Ha and G. Lu. A review of recent research on bio-inspired structures and materials for energy absorption applications. *Composites Part B: Engineering*, **181**, (2020). https://doi.org/10.1016/j.compositesb.2019.107496.

[4] D. Asprone, F. Auricchio, C. Menna, and V. Mercuri. 3D printing of reinforced concrete elements: Technology and design approach. *Construction and Building Materials*, **165**, (2018), pp. 218–231. https://doi.org/10.1016/j.conbuildmat.2018.01.018.

[5] V. Nguyen-Van, B. Panda, G. Zhang, H. Nguyen-Xuan, and P. Tran. Digital design computing and modelling for 3-D concrete printing. *Automation in Construction*, **123**, (2021). https://doi.org/10.1016/j.autcon.2020.103529.

[6] P. D. Nguyen, T. Q. Nguyen, Q. B. Tao, F. Vogel, and H. Nguyen-Xuan. A data-driven machine learning approach for the 3D printing process optimisation. *Virtual and Physical Prototyping*, (2022), pp. 1–19. https://doi.org/10.1080/17452759.2022.2068446.

[7] D.-W. Lee, K. A. Khan, and R. K. Abu Al-Rub. Stiffness and yield strength of architectured foams based on the Schwarz Primitive triply periodic minimal surface. *International Journal of Plasticity*, **95**, (2017), pp. 1–20. https://doi.org/10.1016/j.ijplas.2017.03.005.

[8] D. W. Abueidda, R. K. Abu Al-Rub, A. S. Dalaq, D.-W. Lee, K. A. Khan, and I. Jasiuk. Effective conductivities and elastic moduli of novel foams with triply periodic minimal surfaces. *Mechanics of Materials*, **95**, (2016), pp. 102–115. https://doi.org/10.1016/j.mechmat.2016.01.004.

[9] M. M. Sychov, L. A. Lebedev, S. V. Dyachenko, and L. A. Nefedova. Mechanical properties of energy-absorbing structures with triply periodic minimal surface topology. *Acta Astronautica*, **150**, (2018), pp. 81–84. https://doi.org/10.1016/j.actaastro.2017.12.034.

[10] I. Maskery, N. T. Aboulkhair, A. O. Aremu, C. J. Tuck, and I. A. Ashcroft. Compressive failure modes and energy absorption in additively manufactured double gyroid lattices. *Additive Manufacturing*, **16**, (2017), pp. 24–29. https://doi.org/10.1016/j.addma.2017.04.003.

[11] O. Al-Ketan, R. Rowshan, and R. K. Abu Al-Rub. Topology-mechanical property relationship of 3D printed strut, skeletal, and sheet based periodic metallic cellular materials. *Additive Manufacturing*, **19**, (2018), pp. 167–183. https://doi.org/10.1016/j.addma.2017.12.006.

[12] L. Yang, C. Yan, C. Han, P. Chen, S. Yang, and Y. Shi. Mechanical response of a triply periodic minimal surface cellular structures manufactured by selective laser melting. *International Journal of Mechanical Sciences*, **148**, (2018), pp. 149–157. https://doi.org/10.1016/j.ijmecsci.2018.08.039.

[13] P. Tran and C. Peng. Triply periodic minimal surfaces sandwich structures subjected to shock impact. *Journal of Sandwich Structures & Materials*, **23**, (6), (2020), pp. 2146–2175. https://doi.org/10.1177/1099636220905551.

[14] C. Peng and P. Tran. Bioinspired functionally graded gyroid sandwich panel subjected to impulsive loadings. *Composites Part B: Engineering*, **188**, (2020). https://doi.org/10.1016/j.compositesb.2020.107773.

[15] H. Nguyen-Xuan, K. Q. Tran, C. H. Thai, and J. Lee. Modelling of functionally graded triply periodic minimal surface (FG-TPMS) plates. *Composites Structures*, (2023). (Manuscript submitted for publication).

[16] B.-L. Dang, V. Nguyen-Van, P. Tran, M. A. Wahab, J. Lee, K. Hackl, and H. Nguyen-Xuan. Mechanical and hydrodynamic characteristics of emerged porous Gyroid breakwaters based on triply periodic minimal surfaces. *Ocean Engineering*, **254**, (2022). https://doi.org/10.1016/j.oceaneng.2022.111392.

[17] V. Nguyen-Van, N. K. Choudhry, B. Panda, H. Nguyen-Xuan, and P. Tran. Performance of concrete beam reinforced with 3D printed Bioinspired primitive scaffold subjected to three-point bending. *Automation in Construction*, **134**, (2022). https://doi.org/10.1016/j.autcon.2021.104060.

[18] V. Nguyen-Van, J. Liu, C. Peng, G. Zhang, H. Nguyen-Xuan, and P. Tran. Dynamic responses of bioinspired plastic-reinforced cementitious beams. *Cement and Concrete Composites*, **133**, (2022). https://doi.org/10.1016/j.cemconcomp.2022.104682.

[19] H. Adeli. Neural Networks in Civil Engineering: 1989–2000. *Computer-Aided Civil and Infrastructure Engineering*, **16**, (2), (2001), pp. 126–142. https://doi.org/10.1111/0885-9507.00219.

[20] S. Lee, J. Ha, M. Zokhirova, H. Moon, and J. Lee. Background information of deep learning for structural engineering. *Archives of Computational Methods in Engineering*, **25**, (1), (2018), pp. 121–129. https://doi.org/10.1007/s11831-017-9237-0.

[21] C. Bai, H. Nguyen, P. G. Asteris, T. Nguyen-Thoi, and J. Zhou. A refreshing view of soft computing models for predicting the deflection of reinforced concrete beams. *Applied Soft Computing*, **97**, (2020). https://doi.org/10.1016/j.asoc.2020.106831.

[22] M. Shariati, M. S. Mafipour, P. Mehrabi, A. Shariati, A. Toghroli, N. T. Trung, and M. N. A. Salih. A novel approach to predict shear strength of tilted angle connectors using artificial intelligence techniques. *Engineering with Computers*, **37**, (3), (2020), pp. 2089–2109. https://doi.org/10.1007/s00366-019-00930-x.

[23] H. Nguyen, T. Vu, T. P. Vo, and H.-T. Thai. Efficient machine learning models for prediction of concrete strengths. *Construction and Building Materials*, **266**, (2021). https://doi.org/10.1016/j.conbuildmat.2020.120950.

[24] Q. X. Lieu, K. T. Nguyen, K. D. Dang, S. Lee, J. Kang, and J. Lee. An adaptive surrogate model to structural reliability analysis using deep neural network. *Expert Systems with Applications*, **189**, (2022). https://doi.org/10.1016/j.eswa.2021.116104.

[25] L. C. Nguyen and H. Nguyen-Xuan. Deep learning for computational structural optimization. *ISA Trans*, **103**, (2020), pp. 177–191. https://doi.org/10.1016/j.isatra.2020.03.033.

[26] L. Han and S. Che. An overview of materials with triply periodic minimal surfaces and related geometry: From biological structures to self-assembled systems. *Adv Mater*, **30**, (17), (2018). https://doi.org/10.1002/adma.201705708.

[27] A. H. Schoen. Infinite periodic minimal surfaces without self-intersections. Report, (1970).

[28] S. Rajagopalan and R. A. Robb. Schwarz meets Schwann: design and fabrication of biomorphic and durataxic tissue engineering scaffolds. *Med Image Anal*, **10**, (5), (2006), pp. 693–712. https://doi.org/10.1016/j.media.2006.06.001.

[29] O. Al-Ketan and R. K. Abu Al-Rub. Multifunctional mechanical metamaterials based on triply periodic minimal surface lattices. *Advanced Engineering Materials*, **21**, (10), (2019). https://doi.org/10.1002/adem.201900524.

[30] F. S. L. Bobbert, K. Lietaert, A. A. Eftekhari, B. Pouran, S. M. Ahmadi, H. Weinans, and A. A. Zadpoor. Additively manufactured metallic porous biomaterials based on minimal surfaces: A unique combination of topological, mechanical, and mass transport properties. *Acta Biomaterialia*, **53**, (2017), pp. 572–584. https://doi.org/10.1016/j.actbio.2017.02.024.

[31] C. Peng, K. Fox, M. Qian, H. Nguyen-Xuan, and P. Tran. 3D printed sandwich beams with bioinspired cores: Mechanical performance and modelling. *Thin-Walled Structures*, **161**, (2021). https://doi.org/10.1016/j.tws.2021.107471.

[32] T. D. Ngo, A. Kashani, G. Imbalzano, K. T. Q. Nguyen, and D. Hui. Additive manufacturing (3D printing): A review of materials, methods, applications and challenges. *Composites Part B: Engineering*, **143**, (2018), pp. 172–196. https://doi.org/10.1016/j.compositesb.2018.02.012.

[33] B. Zhou, R. Wu, S. Lu, and S. Yin. A general numerical model for predicting the flexural behavior of hybrid FRP-steel reinforced concrete beams. *Engineering Structures*, **239**, (2021). https://doi.org/10.1016/j.engstruct.2021.112293.

[34] T. Poltue, C. Karuna, S. Khrueaduangkham, S. Seehanam, and P. Promoppatum. Design exploration of 3D-printed triply periodic minimal surface scaffolds for bone implants. *International Journal of Mechanical Sciences*, **211**, (2021). https://doi.org/10.1016/j.ijmecsci.2021.106762.

[35] M. Hafezolghorani, F. Hejazi, R. Vaghei, M. S. B. Jaafar, and K. Karimzade. Simplified damage plasticity model for concrete. *Structural Engineering International*, **27**, (1), (2018), pp. 68–78. https://doi.org/10.2749/101686616x1081.

[36] Z. Sun, D.-C. Feng, Y. Sun, J. Yuan, X. Li, and Y. Wei. Bond-slip behavior of bundled steel/FRP bars and its implementation in high-fidelity FE modeling of reinforced concrete beams. *Construction and Building Materials*, **286**, (2021). https://doi.org/10.1016/j.conbuildmat.2021.122887.

[37] V. Nguyen-Van, P. Tran, C. Peng, L. Pham, G. Zhang, and H. Nguyen-Xuan. Bioinspired cellular cementitious structures for prefabricated construction: Hybrid design & performance evaluations. *Automation in Construction*, **119**, (2020). https://doi.org/10.1016/j.autcon.2020.103324.

[38] I. A. Basheer and M. Hajmeer. Artificial neural networks: fundamentals, computing, design, and application. *Journal of Microbiological Methods*, **43**, (1), (2000), pp. 3–31. https://doi.org/10.1016/S0167-7012(00)00201-3.

[39] U. Simsek, A. Akbulut, C. E. Gayir, C. Basaran, and P. Sendur. Modal characterization of additively manufactured TPMS structures: comparison between different modeling methods. *The International Journal of Advanced Manufacturing Technology*, **115**, (3), (2020), pp. 657–674. https://doi.org/10.1007/s00170-020-06174-0.

[40] T. Le-Duc, Q. H. Nguyen, J. Lee, and H. Nguyen-Xuan. Strengthening gradient descent by sequential motion optimization for deep neural networks. *IEEE Transactions on Evolutionary Computation*, (2022). https://doi.org/10.1109/TEVC.2022.3171052.

[41] E. Samaniego, C. Anitescu, S. Goswami, V. M. Nguyen-Thanh, H. Guo, K. Hamdia, X. Zhuang, and T. Rabczuk. An energy approach to the solution of partial differential equations in computational mechanics via machine learning: Concepts, implementation and applications. *Computer Methods in Applied Mechanics and Engineering*, **362**, (2020). https://doi.org/10.1016/j.cma.2019.112790.